Quantifying the intensity of crystallographic preferred orientation (CPO): some practical considerations and recommended practices

A. J. Cross[1*]

[1]*Department of Geology and Geophysics, Woods Hole Oceanographic Institution, Woods Hole, MA, USA*

**Corresponding author (e-mail: across@whoi.edu)*

Abstract

Crystallographic preferred orientations (CPOs) commonly develop during the crystal-plastic deformation of rocks and minerals, and are widely used to infer strain intensity and geometry, reconstruct deformation conditions, and estimate mechanical anisotropy. Although CPO intensity is often quantified using scalar metrics that reduce the full orientation distribution to a single value, these measures can be highly sensitive to their calculation parameters and input data quality. Here, we examine the performance of two widely used metrics—the J-index and the M-index—using orientation data from a diverse suite of simulated, natural, and experimental specimens. We show that ODF-based measures of CPO intensity such as the J-index (and the ODF-derived variant of the M-index) can vary markedly with kernel parameters and may not converge to a unique value without careful treatment. In contrast, the M-index yields stable, reproducible results across a broad range of conditions when calculated in its original form using random-pair misorientation angle histograms. Monte Carlo resampling shows that M can be accurately estimated with 95% probability using ~500 orientations for moderate-to-strong CPOs ($M \geq 0.25$), whereas weak CPOs ($M < 0.1$) may require up to ~3,000 unique orientation

measurements. These results highlight the inherent limitations of reducing complex orientation distributions to one-dimensional metrics, and underscore the importance of consistent methodology, adequate sampling, and transparent reporting. Consequently, we propose a set of practical guidelines to improve the robustness, reproducibility, and comparability of CPO intensity estimates among specimens of similar type, mineralogy, and origin.

1. Introduction

At elevated pressures and temperatures, crystalline materials—including rocks and minerals—often deform via crystal-plastic mechanisms that produce a rotation and/or alignment of their constituent crystals. For instance, when deformation is mediated by dislocation motion, grains will rotate into orientations that maximize dislocation glide and the shear stresses resolved on their weakest crystal lattice planes (Andrade & Roscoe, 1937), producing a crystallographic preferred orientation (CPO) defined by the alignment of certain crystal axes relative to the bulk kinematic flow. Under such conditions, the crystallographic direction corresponding to the dislocation glide vector (i.e., the Burgers vector) will tend to rotate toward the maximum principal stretching direction, while the corresponding glide plane evolves toward an orientation that maximizes resolved shear stress within the instantaneous stress field. Thus, CPO geometry commonly reflects the symmetry and orientation of the imposed deformation field.

Although CPO development is often attributed to deformation by dislocation creep (e.g., Tullis, 1979; Karato, 1988; Fliervoet et al., 1999), there is also a growing body of literature demonstrating that modest CPOs may develop during dislocation-accommodated grain

boundary sliding (disGBS) in olivine (Hansen et al., 2011; Precigout & Hirth, 2014), quartz (Cross et al., 2017a; Tokle et al., 2019), calcite (Rutter et al., 1994; Pozzi et al., 2019; Demurtas et al., 2019), ice (Thomas et al., 2024), and plagioclase (Miranda et al., 2016). In contrast, deformation via diffusive mass transfer is often found to systematically weaken, or perhaps even entirely randomize, a pre-existing CPO (Boullier & Guergen, 1975; Zhang et al., 1994; Wheeler, 2009; Cross & Skemer, 2017), although several exceptions to this have also been identified (Bons & den Brok, 2000; Barreiro et al., 2007; Sundberg & Cooper, 2008; Miyazaki et al., 2013; Soda et al., 2019). Other processes that may form or modify CPO include deformation twinning (e.g., Tullis, 1970; Barber & Wenk, 1979), cataclasis (Demurtas et al., 2019), metamorphic reactions (Gilgannon et al., 2024), and polymorphic phase transitions (Goddard et al., 2025).

Regardless of the precise mechanisms responsible for their development, CPOs exert a major influence over the mechanical properties and geophysical signatures of deformed rocks. Given that CPOs often arise from the alignment of easy-slip crystal lattice planes during deformation, the presence of a strong CPO can impart significant viscous anisotropy, whereby a material flows more readily in certain orientations than in others. Polycrystalline olivine, for instance, is up to ~15 times weaker when deformed in an orientation that maximizes shear stress on the (010)[100] slip system, versus in an orientation normal to that slip system (Hansen et al., 2012). Similarly, "enhancement" factors of up to 17 have been found for polycrystalline ice deforming via basal (0001) slip (Shoji & Langway Jr., 1988). Thus, CPO development is widely thought to impart progressive weakening—and influence strain localization—during the viscous flow of Earth's

lithosphere (e.g., Bystricky et al., 2000; Skemer et al., 2013) and cryosphere (e.g., Azuma, 1994; Fan et al., 2021a). Meanwhile, CPOs also produce elastic anisotropy that gives rise to seismic anisotropy, a common means for inferring the magnitude and direction of viscous flow in ice sheets (e.g., Smith et al., 2017), the lower crust (e.g., Mainprice & Nicolas, 1989) and the upper mantle (see Karato et al., 2008; Skemer & Hansen, 2016).

2. Scalar CPO intensity metrics: The *J*- and *M*-index

Given the rheological, structural, and geophysical importance of mineral anisotropy, there has long been interest in quantifying CPO intensity, and its evolution, in exhumed natural shear zones and in experimental specimens. Although a population of crystal orientations can most accurately be described using a continuous, harmonic, probability density function—the orientation density function (ODF)—it is often desirable to represent CPO strength using a single, scalar value. Arguably the most widely used of these metrics is the *J*-index, defined as the L^2-norm of the ODF or, in plainer terms, as the sum of the squared orientation density over the ODF (Bunge, 1982):

$$J_{\mathrm{ODF}} = \|f\|_{L^2}^2 = \int |f(g)|^2 \, \mathrm{d}g \tag{1}$$

where $f(g)$ represents the ODF for a population of orientations, g.

The *J*-index ranges from 1 for a uniform orientation distribution to infinity for a single orientation, and can therefore be ambiguous in terms of what qualifies as a "strong" or "weak" CPO. Furthermore, because the ODF is defined over the symmetry-reduced fundamental region of *SO(3)* orientation space, which occupies a larger volume for low-symmetry crystal systems, phases with lower symmetry (e.g., triclinic) will naturally exhibit larger J values than high-symmetry phases (e.g., cubic) for comparable orientation concentration, unless a correction is made for the difference in *SO(3)* volume (e.g., Mainprice et al., 2015).

As an alternative, Skemer et al. (2005) proposed the misorientation index, *M*-index, defined as the difference between the random-pair (uncorrelated) misorientation-angle distribution (MAD) expected for a random orientation population of a given crystal symmetry class, R^0, and the random-pair MAD measured for a given sample, R^T:

$$M = \frac{1}{2}\int |R^T(\theta) - R^0(\theta)|\,\mathrm{d}\theta \tag{2}$$

where θ is misorientation angle. As a reminder, the random-pair MAD is obtained by calculating the misorientation angle between every possible pair of orientations in a particular population—though in practice a subset of orientation pairs is typically sampled for computational efficiency—as opposed to the neighbour-pair MAD, which uses the misorientation angle only between orientation pairs measured adjacent to one another in Euclidean (sample coordinate)

space. Thus, as CPO develops and grains become more strongly aligned, their random-pair MAD will progressively deviate from the theoretical MAD by migrating towards smaller misorientation angles (Wheeler et al., 2001). The *M*-index varies from 0 for a randomly oriented aggregate (i.e., with complete overlap between R^0 and R^T) to 1 for a single orientation (i.e., with no overlap between R^0 and R^T).

In its original form, the M-index was calculated using a histogram of the random-pair MAD—that is, with measurements discretized into bins of a finite width, typically 1° (Skemer et al., 2005):

$$M_{\mathrm{MAD}} = \frac{\theta_{\max}}{2n} \sum_{i=1}^{n} \left| R_i^T - R_i^0 \right| \mathrm{d}\theta \tag{3}$$

where θ_{max} is the maximum misorientation angle for a given crystal symmetry class, and n is the number of bins. While Skemer *et al.* demonstrated that the *M*-index is insensitive to bin width up to (and including) a bin size of 40°, Mainprice et al. (2015) proposed an alternative, continuous variant of the *M*-index, M_{ODF}, calculated from the measured and uniform ODFs, $f^{\mathrm{M}}(\theta)$ and $f^{\mathrm{U}}(\theta)$, respectively:

$$M_{\mathrm{ODF}} = \frac{1}{2} \int \left| f^U(\theta) - f^M(\theta) \right| \mathrm{d}\theta \tag{4}$$

It is this formulation of the *M*-index that is currently implemented in the widely used open-source MTEX toolbox (Bachmann et al., 2010).

3. Limitations and critiques of scalar CPO intensity metrics

Although scalar CPO metrics are often treated—implicitly or explicitly—as quantitative measures of an intrinsic material property, it is important to recognize that any such metric represents a severe dimensional reduction of the underlying orientation distribution. In the most complete sense, CPO represents a three-dimensional probability density function defined over orientation space, *SO(3)*, whereas scalar indices collapse that information into a single value by integrating, differentiating, or otherwise projecting the distribution onto a one-dimensional measure. Inevitably, this process discards information about the shape, symmetry, and topology of the ODF, meaning that distinct orientation distributions may yield identical scalar intensities. For example, note that a perfect [100]-fibre texture in the orthorhombic ("mmm") crystal system can produce an M-index value no greater than 0.436—a value that would otherwise correspond to a unimodal ODF of relatively modest strength. This limitation is not unique to the M-index: scalar CPO metrics in general, including the J-index, depend on *how* orientation density is distributed in *SO(3)*, not solely on the *degree* of crystallographic alignment. Scalar CPO metrics should therefore be understood not as complete mathematical descriptors of orientation distributions, but as heuristic quantities that facilitate comparison among similar datasets, provided that their limitations and sensitivities are explicitly acknowledged.

148 It is precisely this unavoidable loss of information that underlies a long-standing debate over
149 how CPO intensity should be quantified in practice. To date, efforts to quantify CPO intensity
150 using a single scalar metric have coalesced around two broad schools of thought, emphasizing
151 statistical rigor on the one hand and practical utility on the other. Notably, Skemer et al. (2005)
152 previously argued that ODF-based measures such as the J-index can be highly sensitive to data
153 population size and numerical choices associated with ODF construction (e.g., bandwidth,
154 Gaussian halfwidth), motivating the development of the M-index as an ostensibly more robust,
155 parameter-insensitive alternative. However, in a subsequent commentary, Schaeben (2007)
156 countered that *all* scalar measures of CPO intensity—including the M-index—are intrinsically
157 limited in their own ways for the reasons described above.
158
159 Responding to the specific criticism that J systematically decreases as a function of N (the
160 number of orientation measurements), Schaeben (2007) emphasized that this bias is a natural
161 consequence of estimation variance within a finite population rather than a conceptual flaw of
162 the J-index itself. As an extreme example, consider the case in which we have a uniform
163 distribution of N orientations. If we were to construct an ODF for just $n = 1$ measurement taken
164 at random, that ODF would effectively exhibit a monodisperse (i.e., single-crystal) distribution,
165 with $J \rightarrow \infty$. More generally, an ODF constructed from a limited number of measurements will
166 naturally feature a low signal-to-noise ratio, producing spurious ODF peaks that, when squared
167 and summed (Equation 1), will yield an artificially large value of J. As n increases and the
168 orientation distribution is sampled more comprehensively, the signal-to-noise ratio will improve,

169 allowing a more coherent signal to emerge that is dominated by genuine features of the
170 underlying orientation distribution. This effect, termed the 1/*n* law, is examined in detail by
171 Matthies & Wagner (1996), who show that sufficient sampling of the orientation distribution
172 produces approximately linear behaviour over a broad range of *J* versus 1/*n*. By extrapolating
173 this relationship to 1/*n* = 0 (i.e., *n* = ∞), it is thus possible to obtain the "true" value of *J*.
174 Furthermore, Schaeben (2007) argues that while the variance of *J* can be rigorously estimated
175 using (geo)statistical approaches that account for spatial correlation among orientations (e.g.,
176 Boogaart, 2001), similar evaluation for the M-index is less straightforward because it is based on
177 a reduced representation of the data (i.e., the misorientation angle distribution).
178
179 In addressing Schaeben's (2007) criticisms, Skemer & Karato (2007) clarified that the M-index
180 was designed not to replace the J-index but, rather, to provide a complementary measure of
181 CPO intensity that is more practical for Earth-science applications, both by requiring fewer
182 corrections to account for undersampling (c.f., Matthies & Wagner, 1996) and by giving a more
183 stable result for limited numbers of measurements, albeit at the cost of mathematical rigour. For
184 example, as highlighted by Wenk (2002), unless an impractically large number of grains are
185 measured (*N* = 181,584 for complete sampling of a uniform orientation distribution at 5° ODF
186 resolution), the orientation distribution must be faithfully interpolated using a smoothing (e.g.,
187 Gaussian) function, the ideal halfwidth of which is not known *a priori*, and which will depend on
188 CPO intensity, CPO type/symmetry, and the measured number of orientations. Whereas a typical
189 46 × 26 mm polished thin section might contain only ~6,000 individual grains of 0.5-mm

diameter, that same specimen would yield ~18 million random-pair misorientations even if only one orientation measurement per grain is considered. Furthermore, while the M-index also exhibits a 1/*n*-type variance, Skemer et al. (2005) report that a stable value is obtained for as few as 150–600 orientation measurements (corresponding to just 17–35 individual grain measurements in the example provided above).

4. Objectives

Despite the extensive discussion outlined above, CPO intensity is currently quantified using a wide range of approaches across the Earth-science community. These methodological choices—often guided more by convention or convenience than by a clear understanding of the various sensitivities and limitations involved—can lead to substantial variability among otherwise comparable datasets, complicating efforts to interpret the microphysical processes responsible for CPO development and modification. Although important foundations for rigorously quantifying CPO intensity have already been laid (e.g., Matthies & Wagner, 1996; Wenk, 2002; Skemer et al., 2005; Schaeben, 2007), these issues have so far only been addressed in a limited or fragmented manner, often focusing on single metrics, specific crystal symmetry classes, and/or isolated datasets.

The primary objectives of this contribution are, thus, threefold. First, to demonstrate the sensitivity of common CPO intensity metrics to their calculation parameters. Second, to determine the number of measurements required to obtain a stable, robust value of CPO

intensity for a broad spectrum of simulated, experimental, and natural specimens. Finally, to establish some guiding principles and best practices for quantifying and reporting CPO intensity.

Although the present study relies heavily on orientation data collected using EBSD, the findings should, in principle, be applicable to orientation data obtained using any microanalytical or numerical method from which the complete crystal orientation is derived (e.g., excluding polarized-light analyses from which only the optic-axis orientation is provided). Likewise, although we shall focus exclusively on the J- and M-index as these are by far the most widely used CPO-intensity metrics within the Earth-science community, similar principles should apply to other scalar metrics derived from the complete ODF; for example, those based on component volume (e.g., Hielscher et al., 2010) or ODF entropy (Schaeben, 1988). Meanwhile, certain other metrics shall be omitted entirely—specifically, those based on eigenvalue decomposition of the ODF (Woodcock, 1977; Vollmer, 1990), or maximum pole figure intensity, as those methods must be calculated for individual crystal axes rather than for the ODF as a whole and, as such, provide an incomplete view of CPO intensity.

To be clear, the purpose of this manuscript is not to propose a single unifying method or metric for quantifying CPO intensity. Such an endeavour is at best exceedingly difficult, if not impossible, given the aforementioned limitations of using scalar methods to represent three-dimensional distributions—indeed, as we shall see below, CPO "intensity" is highly sensitive to crystal symmetry class, CPO shape/symmetry, deformation geometry, and strain history.

Deriving a method that accounts and corrects for all of these differences is beyond the scope of the present study. Instead, it is hoped that this work will bring attention to the various sensitivities and options regarding CPO measurement, thereby enabling the reader to make more deliberate and informed choices regarding the rigorous quantification, reporting, and comparison of CPO evolution among like-phases and similar settings.

5. Performance of the J- and M-indices for synthetic data

5.1. Single crystals

As a starting point, we can examine how the *J*-index and *M*-index respond to the end-member case of a monodisperse (i.e., single-crystal) orientation distribution. Figure 1 shows J_{ODF} and M_{ODF} as a function of ODF halfwidth and bandwidth for several crystal-symmetry classes. The halfwidth—defined as the half-width at half-height of the kernel function used to construct the ODF—dictates the "sharpness" of the ODF. Larger halfwidth values emphasize broad, long-wavelength features, whereas smaller halfwidth values provide more sensitivity to local, short-wavelength features. Bandwidth, meanwhile, represents the highest harmonic order (i.e., highest angular-frequency band) used to represent the ODF. As bandwidth increases, the number of terms used to fit the ODF to a population of orientations increases, allowing local variations in orientation density to be captured with greater fidelity—see Supplementary Figure S1 for example pole figures.

As highlighted by Skemer et al. (2005), J_{ODF} varies continuously over the entire parameter space, being relatively insensitive to bandwidth but highly sensitive to the ODF kernel halfwidth (Figure 1, top row). At large halfwidth values (20–40°), J_{ODF} approaches unity; that is, the value expected for a random orientation distribution (recall that these calculations are for monodisperse, single-crystal CPO). However, as halfwidth decreases to 2°, J_{ODF} increases over several orders of magnitude. The maximum magnitude of J_{ODF} also increases as crystal symmetry decreases, from 10^4 for cubic crystals to 10^5 for triclinic crystals, highlighting that CPO intensity cannot easily be compared among phases belonging to different crystal systems unless extra care is taken to normalize the results (e.g., Mainprice et al., 2015).

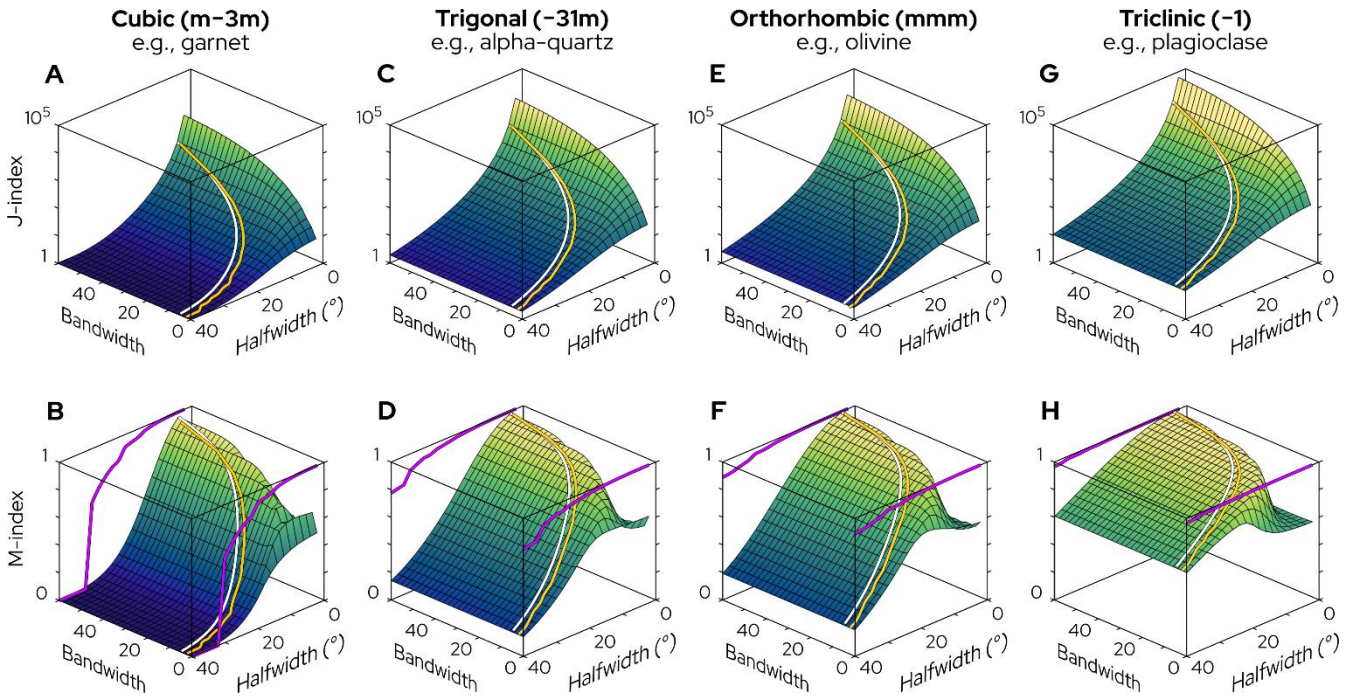

Figure 1: *J*-index (top row; Equation 1) and *M*-index (bottom row; Equation 4) as a function of ODF bandwidth and halfwidth for single orientations of A–B) cubic, C–D) trigonal, E–F) orthorhombic, and G–H) triclinic phases. The white curves indicate the conditions under which the three highest-order harmonic bands contribute negligible power, as determined from spectral decomposition of the ODF (see Supplementary Figure S1). The yellow curves show the optimum relationship between halfwidth and bandwidth determined by MTEX. Above this line (i.e., at greater bandwidths), the ODF is effectively oversmoothed and lacks high-order harmonic content, whereas below it, the harmonic representation is truncated and may fail to capture sharp features of the orientation distribution. All ODFs were constructed in MTEX (version 6.1.0) using the default de la Vallee Poussin kernel (Schaeben, 1997). *M*-index values were also calculated using the original, discrete method of Skemer et al. (2005; Equation 3), and are plotted as 1-D curves (purple lines) alongside the M_{ODF} surfaces—for these values, the horizontal axis corresponds to the bin width of the misorientation angle histogram, rather than the ODF halfwidth.

Although halfwidth and bandwidth can be specified individually, it is important to note that they are not truly independent parameters. Halfwidth defines the angular smoothing scale of the ODF, which, in harmonic space, corresponds to a progressive decay of higher-order spectral components (Figure S1, inset), while bandwidth represents the number of spectral components available to represent the ODF. If bandwidth is set too low, the harmonic series is truncated and meaningful high-order structure may be removed; if bandwidth is set too high, high-order components dominated by measurement or numerical noise may be retained. In Figure 1, the boundary between these regimes is approximated by identifying the conditions under which the three highest-order spectral bands of each ODF become negligible (*i.e.*, spectral power ≈ 0). Note also that the range of parameter space shown in Figures 1 and S1 is unrealistically large. In practice, ODF halfwidths commonly fall in the range ≤ 15°, while bandwidths on the order of 100 or more can be chosen with little computational penalty to avoid spectral truncation of the ODF (Schaeben, 2007). Nevertheless, even when halfwidth and bandwidth are treated as co-dependent parameters and are constrained to lie within a relatively narrow range of values, J_{ODF} can still vary over an order of magnitude or more as the ODF halfwidth changes (Figure 1, top row). Thus, substantial effort has been devoted to developing objective, data-driven approaches for selecting an "optimal" kernel halfwidth, with the aim of reducing user discretion and ensuring reproducibility. For example, the default method currently implemented within MTEX relies on a Kullback-Leibler cross-validation approach (Bowman, 1984) whereby candidate halfwidths are

298 evaluated by minimizing the discrepancy between an estimated ODF and a set of withheld
299 orientation data.
300
301 While the *M*-index was originally designed to avoid the shortcomings (i.e., non-uniqueness) of
302 the *J*-index (Skemer et al., 2005), the *M*-index as currently implemented in MTEX—that is, being
303 derived from the ODF (Equation 4) rather than from the MAD (Equation 3)—remains similarly
304 sensitive to ODF halfwidth and bandwidth (Figure 1, bottom row). Notably, M_{ODF} is severely
305 underestimated for halfwidths exceeding 20°, and even for halfwidths in the range 5–15°, falling
306 7–56% below the true value of $M = 1$ for cubic crystals, and 2–25% below $M = 1$ for orthorhombic
307 and trigonal crystals. As halfwidth values of 5–15° are commonly used to calculate ODFs and,
308 thereby, produce contoured pole figures, it is likely that M_{ODF} is widely underestimated when
309 calculated from those same ODFs. Values close to $M_{ODF} = 1$ are obtained only as the ODF
310 halfwidth approaches 2°, yet drop off precipitously at smaller halfwidth values unless a large
311 bandwidth (>>50) is used. In contrast, we find that the original, discrete formulation of the *M*-
312 index (Equation 3) is relatively stable, providing $M_{MAD} \approx 1$ so long as the MAD bin width does
313 not exceed 10° (purple curves on Figure 1, bottom row). The discrete, MAD formulation is
314 therefore more robust—and considerably more computationally efficient—at least for this
315 simple test case.
316
317
318

5.2 Numerical polycrystals

To produce more broadly applicable results, we can now examine CPO intensity for a polycrystalline aggregate featuring varying degrees of crystallographic alignment. Figures 2 and 3 show how *J* and *M* evolve with increasing strain in numerical aggregates of olivine (Figure 2) and ice (Figure 3) subjected to simple-shear deformation using the viscoplastic self-consistent (VPSC) model of Lebensohn & Tomé (1993). The goal of these models is not to produce a fully realistic simulation of CPO evolution—that has been achieved elsewhere using more sophisticated analyses (e.g., Boneh et al., 2015; Hansen et al., 2016; Rathmann et al., 2024)—but, rather, to produce CPOs that span the range from random ($M = 0$; $J = 1$) to strongly unimodal ($M \to 1$; $J \to \infty$). Slip systems and critical resolved shear stresses (CRSS) were chosen to promote the formation of a strong A-type $(010)[100]$ CPO in olivine, and a strong basal-$\langle a \rangle$ $(0001)\langle \bar{1}2\bar{1}0 \rangle$ CPO in ice: both commonly observed in natural settings. Olivine CPO evolution was modelled using six slip systems chosen after Boneh et al. (2015) and Tomassi et al. (2000) to satisfy von Mises' criterion, with two other slip systems—$\{110\}[110]$ and $\{031\}[113]$—added to strengthen the A-type CPO and enable model convergence at large strains. Ice CPO evolution was modelled using the same slip systems employed by Castelnau et al. (1996). The slip systems and their corresponding CRSS values are summarized in Table 1. VPSC simulations were conducted for 20,000 grains—far exceeding the population size needed to obtain a robust estimate of CPO intensity, as shown below—with no neighbour-grain interactions (i.e., co-rotation), and using tangent linearization to validate the Eshelby-type VPSC inclusion scheme (Molinari et al., 1987).

339 The data were subsequently analysed within the MTEX open-source toolbox for MATLAB (MTEX
340 version 6.1.0; Bachmann et al., 2010).

341

342 **Table 1:** Slip systems and CRSS values used for olivine and ice VPSC simulations

Slip system	**CRSS**
Olivine	
$(010)[100]$	1
$(001)[100]$	1
$(010)[001]$	2
$(100)[001]$	3
$\{021\}[100]$	6
$\{110\}[001]$	6
$\{110\}[110]$	10
$\{031\}[113]$	10
Ice	
$(0001)\langle\bar{1}2\bar{1}0\rangle$	1
$\{\bar{1}010\}\langle\bar{1}2\bar{1}0\rangle$	20
$\{11\bar{2}2\}\langle11\bar{2}\bar{3}\rangle$	200

343

344

345 *5.2.1. Halfwidth sensitivity*

346 Figures 2 and 3 show many of the same trends discussed above. At any given strain, J_{ODF} and
347 M_{ODF} decrease with increasing ODF halfwidth (Figures 2D–E, 3D–3E) as the ODF increasingly fails
348 to capture short-wavelength (i.e., low misorientation angle) features (Figures 2C, 3C). In contrast,
349 M_{MAD} monotonically increases along the same trajectory for all MAD bin widths ≤ 10°, spanning
350 the expected range of 0 → 1. In general, M_{ODF} provides values very similar to M_{MAD} for ODF
351 halfwidths of ≤ 5°; however, M_{ODF} decreases significantly at ODF halfwidths greater than 5°
352 (Figures 2E, 3E). Encouragingly, kernel optimisation (i.e., automatic halfwidth, bandwidth
353 selection) via the Kullback-Leibler method yields $M_{ODF} \approx M_{MAD}$ (red line in Figures 2E, 3E), with

354 MTEX selecting an optimal halfwidth that decreases rapidly from ~22° to ~2.5° as strain and
355 CPO intensity increase (Supplementary Figure S2). However, note also that the optimal kernel
356 halfwidth depends on population size, decreasing as the number of orientation measurements
357 increases (Supplementary Figure S2)—see also Bozzolo et al. (2007).
358

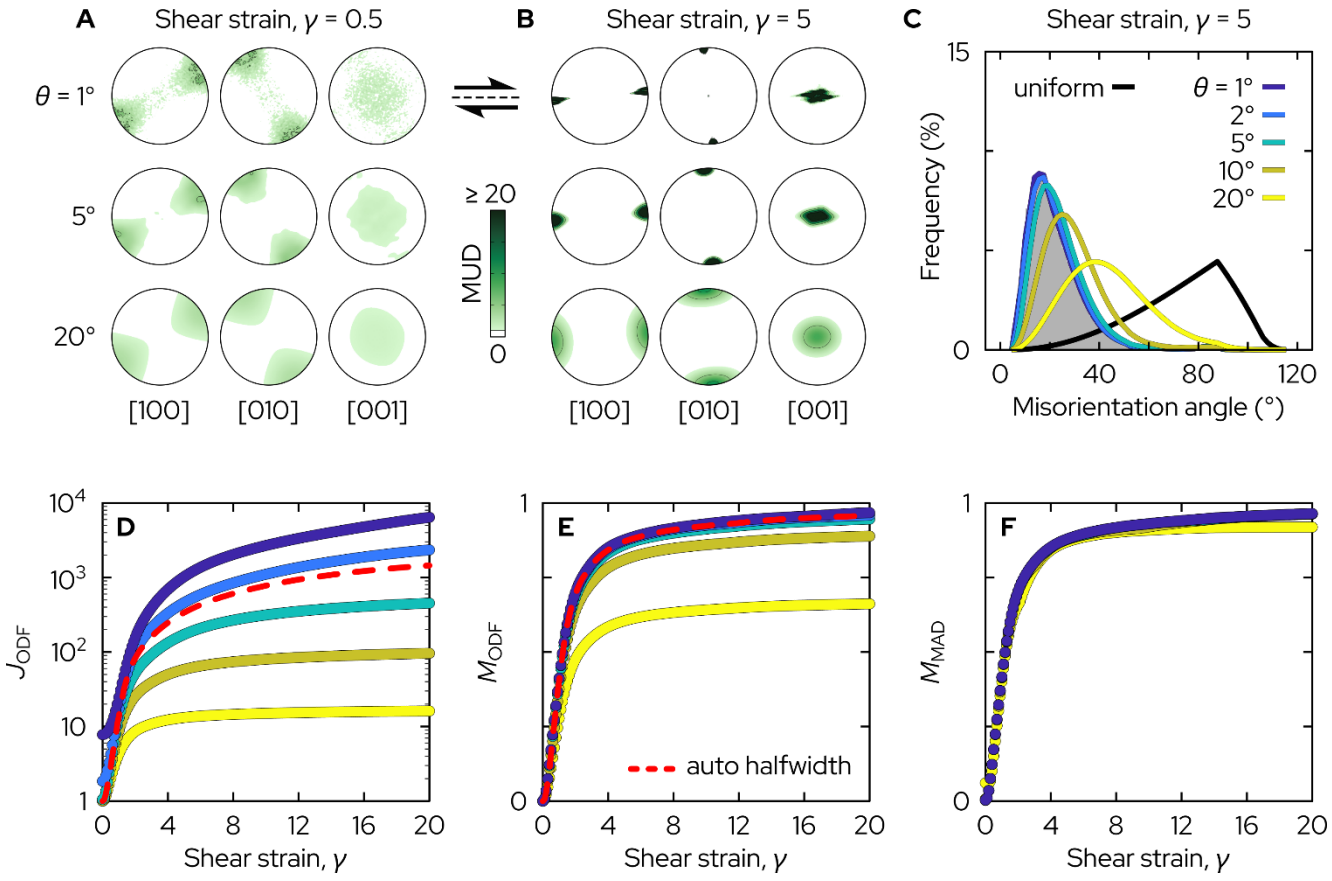

Figure 2: CPO evolution in numerical olivine aggregates undergoing simple shear deformation (see main text for details). (A–B) Contoured pole figures of the [100], [010], and [001] axes at shear strains of (A) γ = 0.5 and (B) γ = 5.0, produced using ODF kernel halfwidths of θ = 1°, 5°, and 20°. (C) The random-pair misorientation angle distribution (MAD) at γ = 5.0 (grey histogram; 2° bin width), alongside misorientation angle distribution functions (MDFs) constructed from ODFs with halfwidths of θ = 1–20° (coloured lines) and the theoretical uniform MDF (black line). Note that the ODF-derived MDFs provide a poor description of the MAD at $\theta \geq 10°$. (D–F) The *J*-, M_{ODF}-, and M_{MAD}-indices as a function of strain for (D–E) ODF halfwidths of 1–20° and (F) MAD bin widths of 1–20°. The red dashed line in (D) and (E) shows *J* and M_{ODF} when the ODF kernel (halfwidth, bandwidth) is chosen automatically using the default MTEX Kullback-Leibler cross-validation approach.

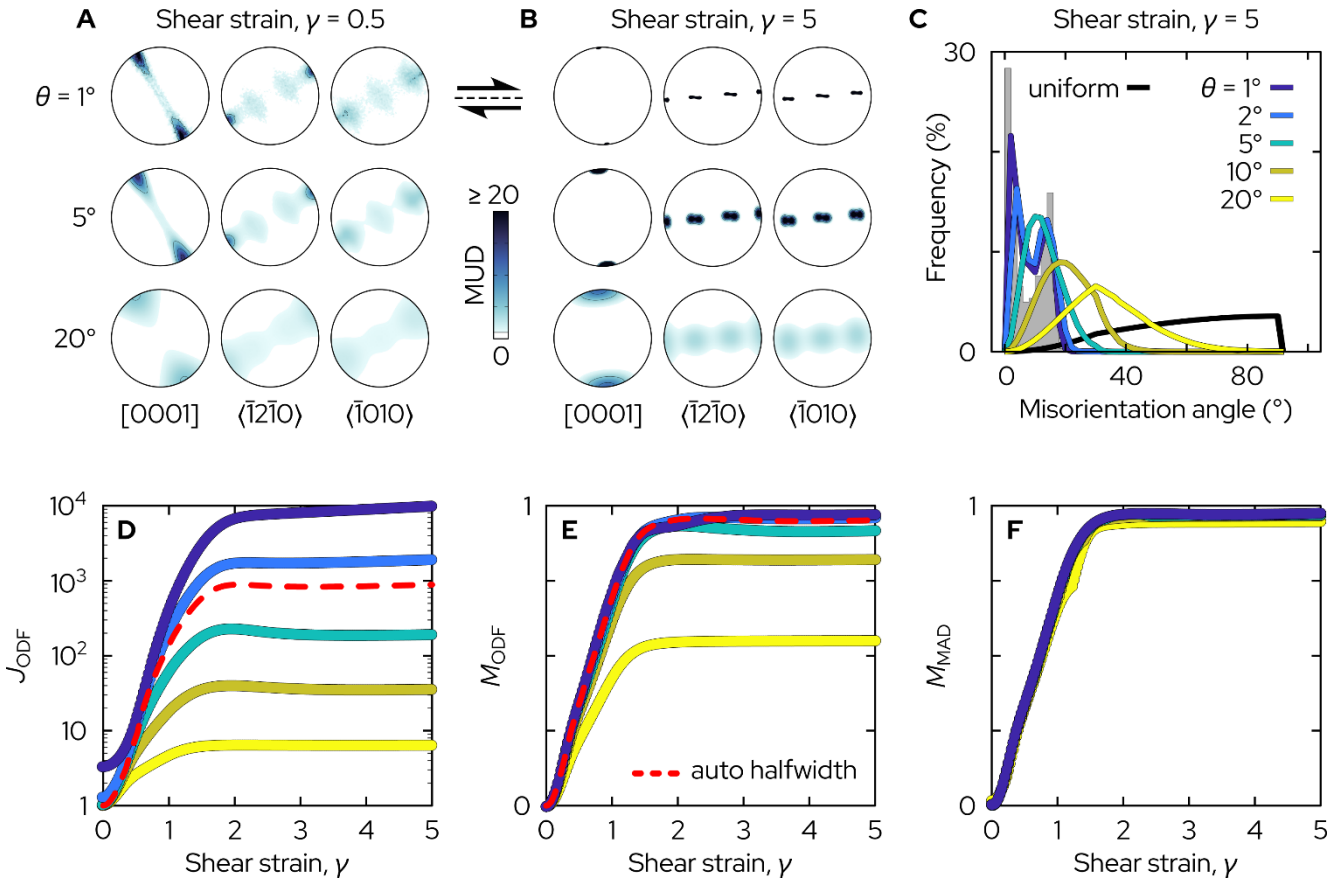

Figure 3: CPO evolution in numerical ice aggregates undergoing simple shear deformation (see main text for details). (A–B) Contoured pole figures of the $[0001]$, $\langle\bar{1}2\bar{1}0\rangle$, and $\langle\bar{1}010\rangle$ axes at shear strains of (A) γ = 0.5 and (B) γ = 5.0, produced using ODF kernel halfwidths of θ = 1°, 5°, and 20°. (C) The random-pair misorientation angle distribution (MAD) at γ = 5.0 (grey histogram; 2° bin width), alongside misorientation angle distribution functions (MDFs) constructed from ODFs with halfwidths of θ = 1–20° (coloured lines) and the theoretical uniform MDF (black line). Note that the ODF-derived MDFs provide a poor description of the MAD at $\theta \geq 5°$. (D–F) The J-, M_{ODF}-, and M_{MAD}-indices as a function of strain for (D–E) ODF halfwidths of 1–20° and (F) MAD bin widths of 1–20°. The red dashed line in (D) and (E) shows J and M_{ODF} when the ODF kernel (halfwidth, bandwidth) is chosen automatically using the default MTEX Kullback-Leibler cross-validation approach.

5.2.2. Parametric versus non-parametric ODF construction

It is worth mentioning that the ODFs analysed in Figures 2 and 3 were all constructed using a parametric Fourier decomposition (i.e., harmonic series expansion) approach in which

$$f_{Fourier}(o) = \sum_{n=0}^{W} \sum_{k=-n}^{n} \sum_{l=-n}^{n} \hat{f}_n^{k,l} \mathrm{D}_n^{k,l}(o) \quad (5)$$

where $o \in SO(3)$ denotes an orientation (rotation matrix) at which the ODF is evaluated in three-dimensional space, $\hat{f}_n^{k,l}$ are the Fourier coefficients, $\mathrm{D}_n^{k,l}$ are the Wigner-D functions that serve as harmonic basis functions in *SO(3)* space (analogous to sines and cosines in classical Fourier series expansion), and *n* is the harmonic degree, with *W* being the truncation order of the expansion; that is, the bandwidth (Hielscher & Schaeben, 2008).

However, ODFs may also be constructed using non-parametric kernel density estimation (KDE) whereby the distribution of orientations in *SO(3)* is described through the superposition (summation) of radially symmetric unimodal model ODFs (kernels) centred around each orientation o_1, o_2, …, o_M:

$$f_{KDE}(o) = \frac{1}{M} \sum_{i=1}^{M} \psi(o o_i^{-1}) \quad (6)$$

where $\psi : SO(3) \rightarrow \mathbb{R}$ is the radially symmetric kernel used to assign a real (scalar) value representing the probability density (e.g., multiples of uniform distribution, MUD) at each orientation in *SO(3)* (Hielscher & Schaeben, 2008). In this approach, the main variables are the functional form of the kernel itself, ψ, and its halfwidth.

In MTEX, the choice between these approaches is made automatically according to internal heuristics such as dataset size, kernel bandwidth, and symmetry. Generally speaking, the KDE-based method is preferred when the ODF contains highly localized, high-intensity features (i.e., for small halfwidths), whereas Fourier-based representation is favoured when the ODF is smoother and can be efficiently represented using a truncated harmonic expansion (i.e., for large halfwidths). However, either approach can be explicitly enforced by the user (as was done for Figures 2 and 3).

To assess the influence of the ODF construction method itself, Figure 4 compares CPO intensity derived using both the Fourier- and KDE-based implementations. In both cases, the MTEX-default de la Vallee Poussin kernel was used (Schaeben, 1997) with the kernel parameters (i.e., halfwidth, bandwidth) selected automatically via Kullback-Leibler cross-validation.

Although both methods converge to similar J_{ODF} (Figures 4A, 4E) and M_{ODF} (Figures 4B, 4F) values at high strain, the KDE-derived values are relatively unstable—despite the VPSC simulations producing highly localized ODFs that are, in principle, best suited to kernel-based

426 representation—evolving erratically, discontinuously, and non-monotonically as a function of
427 strain for the ice simulations in particular (Figures 4E, 4F). In contrast, the Fourier-based ODFs
428 evolve smoothly and strengthen monotonically, with values of M_{ODF} that are almost identical to
429 M_{MAD} at any given strain (dashed line in Figures 4B, 4F). These marked differences are somewhat
430 surprising given the seemingly identical pole figures produced by each method (compare the
431 pole figures outlined in red and blue in Figures 4C, 4G). However, significant local differences
432 are found by subtracting the ODFs from one another: $\Delta(o) = f_{Fourier}(o) - f_{KDE}(o)$ (Figures 4D,
433 4H), with the Fourier-based method producing greater intensity around the primary ODF
434 maximum (red colouring on Figures 4D, 4H) and the KDE-based method capturing the subsidiary
435 features more precisely (blue colouring on Figures 4D, 4H).
436

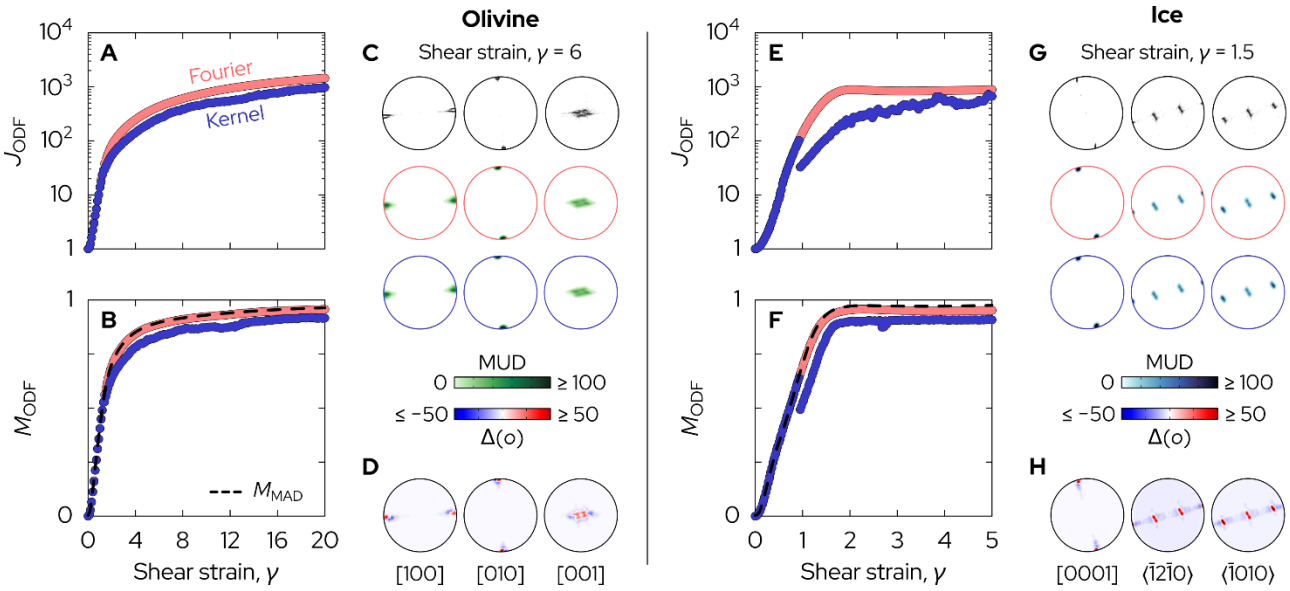

Figure 4: Comparison of parametric (Fourier-based) and non-parametric (KDE-based) ODF construction approaches for the (A–D) olivine and (E–H) ice VPSC simulations. (A, E) J-index and (B, F) M_{ODF}-index as a function of strain. The red data points represent ODFs obtained using Fourier series expansion, whereas the blue data points represent ODFs constructed via the superposition of radially symmetric kernel functions. The dashed black line in (B, F) represents M_{MAD} calculated via the original M-index method of Skemer et al. (2005). (C, G) Equal-area, lower-hemisphere pole figures showing the scattered point data (black outline), Fourier-based contouring (red outline), and kernel-based contouring (blue outline). The difference between the Fourier-based and kernel-based ODFs, $\Delta(o) = f_{Fourier}(o) - f_{KDE}(o)$, is shown in panels (D, H).

6. Sensitivity to population size

6.1 Numerical polycrystals

As a general rule of thumb, it is often assumed that 200–500 measurements are required to obtain a representative estimate of microstructural "state" (e.g., grain size, CPO intensity; Humphreys, 2001; ASTM International, 2013; Cross et al., 2017b). Here, we can test this assumption by directly examining how CPO intensity varies with population size using the VPSC simulations described above.

Figure 5 shows a Monte Carlo resampling analysis of the VPSC results. First, we find the model steps that correspond to 25 evenly spaced M_{MAD} values covering the full range of 0 to 1 (i.e., in increments of ~0.04). Then, for each of those steps, we recalculate M_{MAD} for 1000 random subsamples of orientations at each of 10 different population sizes, spaced evenly in logarithmic space between N = 5 and N = 20,000. Put simply, we recalculate M_{MAD} 250,000 times as a function of CPO intensity and population size. Note that we focus on the M-index as it is difficult to define a singular value of J to use as a reference measure of the "true" CPO intensity at each set of conditions. Furthermore, we focus specifically on M_{MAD} as it is far less computationally expensive than M_{ODF} for the resampling analyses.

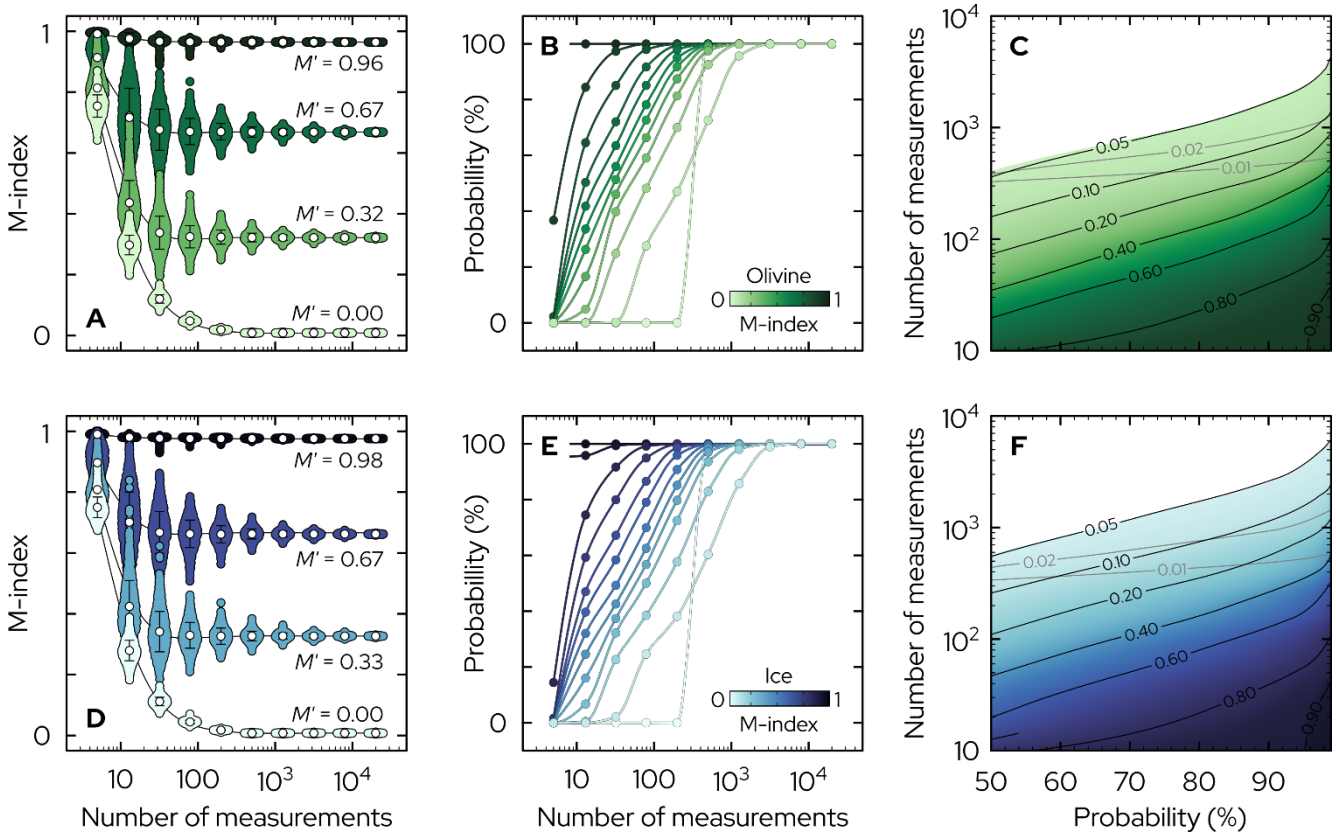

Figure 5: M-index, M_{MAD}, as a function of population size and true CPO intensity, M', for the (A–C) olivine and (D–F) ice VPSC simulations shown above. (A,D) Monte Carlo calculations of M_{MAD} for orientation distributions of varying intensity and size. For each set of conditions, M_{MAD} is calculated using 1,000 random samples of N orientations. To better show the distribution of M_{MAD}, the data points are jittered in the x-direction according to a kernel density estimate along the y-direction. The mean of each distribution is shown by a white circle, with error bars corresponding to the 1-sigma standard deviation. (B,E) The probability of obtaining an estimate of M within 10% of the true CPO intensity, M', as a function of CPO intensity and the number of orientation measurements. (C,F) Contour plots showing the number of orientation measurements required to reach a certain probability of obtaining M within ±10% of M'.

Figures 5A–C and 5D–F show the resampling analysis results for our olivine (Figure 2) and ice (Figure 3) VPSC simulations, respectively. For CPOs of any given intensity, M_{MAD} decreases with increasing population size, converging with the true M_{MAD} value, M', at population sizes on the order of N = 100 to N = 1,000 (Figures 5A and 5D). However, there is much greater relative change in M_{MAD} for weaker CPOs—random orientation distributions ($M' \approx 0$) give M values that, on average, decrease by > 99% (i.e., from ~0.75 to ~0) as N increases, whereas strongly unimodal orientation distributions ($M' \approx 1$) give M values that decrease by only ~3% (i.e., from ~0.99 to ~0.96).

To further quantify these observations, we calculate the probability, P, of obtaining the true value, M', from the normal distribution of M_{MAD} values produced at each set of resampling conditions, within a given degree of acceptable uncertainty, ϵ (i.e., ± 10 % for the following analyses):

$$P(M' - \epsilon \leq M_{\mathrm{MAD}} \leq M' + \epsilon) \tag{7}$$

where P is calculated using the cumulative distribution function (CDF) of a normal distribution, φ_M—with mean, μ_M, and standard deviation, σ_M, describing the distribution of the resampled M_{MAD} values (Figures 5A, 5D)—from z-scores corresponding to the desired bounds, $M' \pm \epsilon$:

$$P = \varphi_M(z_{\mathrm{upper}}) - \varphi_M(z_{\mathrm{lower}})$$

502 (8)

503 where

504 $$z_{\text{upper}} = \frac{M' + \epsilon - \mu_M}{\sigma_M}, \qquad z_{\text{lower}} = \frac{M' - \epsilon - \mu_M}{\sigma_M}$$

505 (9)

506 For example, Figure 5A shows that resampling an A-type olivine CPO with M' = 0.32 produces
507 a normal distribution of M_{MAD} values with mean, μ_M = 0.437 and standard deviation, σ_M =
508 0.0730 when only 13 orientation measurements (i.e., 78 unique misorientation pairs) are
509 selected at random each time. Thus, the probability of obtaining M' = 0.32 ± 0.032 (i.e., M' ±
510 10%) is given by the z-scores, $z_{\text{upper}} = -1.164$ and $z_{\text{lower}} = -2.041$, corresponding to P = 0.105.
511 In other words, there is a ~10.5% chance of obtaining an accurate value of M_{MAD} (i.e., within
512 ±10% of M') when describing that CPO using N = 13 arbitrary orientation measurements. It is
513 not until N > 351 that M' can be obtained with >95% likelihood from a single sample of
514 orientations.

515

516 Figures 5B and 5E show the probability of obtaining M_{MAD} within ±10% of M' when sampling
517 orientation distributions of varying CPO intensities and with varying numbers of
518 measurements. To illustrate these data in a more intuitive manner, Figures 5C and 5F present
519 contoured heat maps showing the number of orientation measurements required to obtain a
520 robust measure of M_{MAD} at a particular probability level for various values of M'. Note that little
521 difference is found between the VPSC simulations for olivine and ice, despite the higher
522 symmetry class of the latter.

523

524 Generally speaking, the number of measurements required to obtain an accurate value of
525 M_{MAD} decreases markedly as CPO intensity increases—consider that only a single orientation
526 measurement would be required to describe the CPO intensity of a monodisperse (single
527 crystal) orientation distribution with 100% likelihood of obtaining the true value, M'.
528 Interestingly, very weak but non-random orientation distributions require the largest number
529 of measurements to obtain a robust measure of M_{MAD}—to obtain a value of M_{MAD} with 95%
530 probability of falling within ±10% of M', up to ~2,500 measurements are required for an A-
531 type olivine CPO with M' = 0.05 (Figure 5C) while ~4,000 measurements are required for a
532 basal-⟨a⟩ ice CPO with M' = 0.05 (Figure 5F). For random orientation distributions ($M \approx 0$),
533 there is rapid convergence with M' beyond ~300 measurements (Figures 5B, 5E). These
534 findings are consistent with previous studies showing that the number of measurements
535 required to accurately resolve an ODF decreases with CPO intensity (Wagner et al., 1998), with
536 several thousand orientations often needed to characterise weak CPOs (Jura et al., 1996;
537 Bozzolo et al., 2007). Recent studies have recommended similarly large sample sizes for
538 determining average grain sizes (Lopez-Sanchez & Llana-Funez, 2016; Lopez-Sanchez, 2020).

539

540 6.2 Natural and experimental samples

541 To assess whether the population-size effects identified above are expressed in real materials,
542 we can now perform the same resampling analysis on a diverse suite of natural and experimental
543 specimens spanning a wide range of crystal symmetries, CPO types, and deformation histories.

Eight specimens containing minerals of various crystal symmetry classes have been selected for analysis, as summarized in Table 2. All of the specimens had previously been mapped using EBSD, and were selected for analysis on the basis that they 1) cover a wide range of CPO intensity and symmetry, and 2) contain ≥ 5000 grains to ensure a robust reference measure of CPO.

In order of decreasing CPO intensity, the specimens are as follows:

1) Sample PT303 is an iron-rich olivine polycrystal deformed to a shear strain of $\gamma = 3.9$ in a torsional geometry using a triaxial gas-medium Paterson apparatus at 1200°C, 300 MPa confining pressure, and a rotation rate corresponding to 2.3×10^{-4} s^{-1} shear strain rate at the outer radius of the sample, where a strong A-type CPO is found (Qi et al., 2021);
2) UM1787 is a quartz-rich mylonite from the Garhwal Himalayas, India, composed primarily of quartz, biotite, muscovite, garnet, and ilmenite (Shivaji, 2020). The sample was mapped perpendicular to foliation and parallel to lineation using a ThermoFisher Helios Hydra 5 scanning electron microscope (SEM) equipped with an Oxford Instruments Symmetry S3 EBSD detector at the Marine Biological Laboratory (Woods Hole, MA, USA). Because muscovite and biotite cannot be distinguished reliably using EBSD alone, all mica orientations were indexed using a muscovite match unit but are described here collectively as "mica". Furthermore, due to the relatively weak diffraction patterns produced by mica, the map was re-indexed using Oxford Instruments' MapSweeper pattern matching toolbox using the same procedures described by Hao et al. (2024), with

a cross-correlation coefficient threshold of R = 0.25. Mica exhibits a strong (001)-fibre CPO, with [100] and [010] axes girdled within the foliation plane;

3) Sample PIL267 is a polycrystalline ice sample deformed in a general shear geometry in a cryogenic, triaxial gas-medium apparatus at −30°C and 1.67 × 10^{-5} s^{-1} shear strain rate to a finite shear strain of γ = 1.1 (Fan et al., 2021b). Under these conditions, ice develops a strong (0001)-axis maximum perpendicular to the shear plane, with a subsidiary (0001)-axis maximum rotated ~45° towards the shear direction, to promote dislocation glide on the basal-⟨a⟩ slip system;

4) Sample W1794 is an intermediate-composition plagioclase polycrystal deformed in a general shear geometry using a Tullis-modified Griggs apparatus at 1000°C, 1000 MPa confining pressure, and various shear-strain-rate steps in the range 10^{-6}–10^{-4} s^{-1} (Meyers et al., 2013). The sample was mapped using a Zeiss Sigma variable-pressure SEM equipped with an Oxford Instruments NordlysNano EBSD detector at the University of Otago (Dunedin, New Zealand);

5) DR538-R3 is an abyssal peridotite ultramylonite from the St. Paul's oceanic transform fault in the equatorial Atlantic Ocean. The sample was collected using a human-occupied vehicle during cruise AL170602 onboard the MV *Alucia*, and is composed primarily of olivine, pyroxene, amphibole, spinel, and low-temperature serpentinization and carbonation products (Klein et al., 2024). The sample was mapped using a Zeiss Supra 40VP SEM equipped with an Oxford Instruments Symmetry S1 detector at the Marine Biological Laboratory (Woods Hole, MA, USA). For the most part, DR538-R3 is fine-

grained with a strong A-type CPO, suggestive of dislocation glide on the (010)[100] slip system (Jung & Karato, 2001). However, the mapped portion of DR538-R3 also contains two large olivine porphyroclasts that cover 10% of the scanned region (Supplementary Figure S1).

6) STO-2-03 is a quartz-rich mylonite from the Alpine Fault zone, New Zealand, deformed in a reverse dip-slip transpressional geometry under mid-crustal conditions (Cross et al., 2015). Quartz exhibits an asymmetric type-I cross girdle CPO suggestive of combined basal-⟨a⟩, rhomb-⟨a⟩, and prism-⟨a⟩ slip;
7) Sample LVT128 is a specimen of Carrara marble deformed in a torsional geometry using a Large Volume Torsion (LVT) apparatus at 700°C, ~1.5 GPa confining pressure, and a rotation rate corresponding to a shear strain rate of 4.8×10^{-5} s^{-1} at the outer radius of the sample (Skemer et al., 2025). A maximum shear strain of γ = 3.2 was reached at the outer radius of the sample, where calcite developed a multi-modal CPO consistent with combined slip on the $r^{+}\{10\bar{1}4\}\langle\bar{2}021\rangle$, $r^{-}\{10\bar{1}4\}\langle 20\bar{2}\bar{1}\rangle$, and $c(0001)\langle\bar{1}2\bar{1}0\rangle$ slip systems (Cross & Skemer, 2017);
8) Sample San466 is a fine-grained quartz polycrystal that was formed by pressurizing a quartz single-crystal into the coesite stability field and then back to the α-quartz stability field at a temperature of ~600°C using a Deformation-DIA apparatus (Goddard et al., 2025). The sample has a macroscopically random orientation distribution, but exhibits a distinct crystallographic signature—whereby neighbouring clusters of grains have [c] axes that are misoriented from one another by a ~84° rotation around their common $\{m\}$

606 axis—due to epitaxy across the coesite-quartz phase transformation (Goddard et al.,
607 2025).
608
609 All of the EBSD maps were processed using the open-source MTEX toolbox for MATLAB
610 (Bachmann et al., 2010). For each specimen, a reference M-index value, *M*′, was calculated using
611 the original histogram-based approach of Skemer et al. (2005) and the mean orientation of 5,000
612 grains selected at random. To demonstrate the diverse range of CPO types present in the
613 samples, the eigenvalue method of Vollmer (1990) was also used to classify the extent to which
614 specific crystal axes exhibit point (P), girdle (G), or random (R) distributions. Figure 6A shows the
615 P-G-R distribution of the inferred Burgers vector (i.e., crystal direction parallel to the shear
616 direction and/or lineation, interpreted as the dominant dislocation glide direction) for each
617 sample, while Figure 6B shows the P-G-R distribution of the dominant glide plane (i.e., crystal
618 axis normal to the shear plane and/or foliation). For San466, which was conducted under
619 nominally hydrostatic conditions, the $a\langle 11\bar{2}0\rangle$ direction and $c(0001)$ pole-to-plane were used
620 for consistency with the other quartz-rich sample, STO-2-03. The chosen specimens cover almost
621 the entire P-G-R ternary space (Figures 6A–B) and also span a wide range of CPO intensity from
622 *M*′ ≈ 0 (San466) to *M*′ = 0.44 (PT303) (Figures 6C–J). Although direct comparison of CPO intensity
623 among such diverse texture and sample types is not meaningful in an absolute sense, this range
624 provides a robust framework for evaluating whether the population-size trends observed in the
625 VPSC simulations above are broadly applicable.
626

627 **Table 2: Summary of EBSD data from natural and experimental specimens**

Sample name	Sample type	Phase of interest	Symmetry class	# grains	CPO type	Inferred slip system	*M'*
PT303	Experimental	Olivine	Orthorhombic	6210	Unimodal	A-type; $(010)[100]$	0.440
UM1787	Natural	Mica	Monoclinic	5590	Fibre	C-fibre; $(001)[uv0]$	0.268
PIL267	Experimental	Ice	Hexagonal	21924	Unimodal	Basal-a; $(0001)\langle\bar{1}2\bar{1}0\rangle$	0.217
W1794	Experimental	Plagioclase	Triclinic	6746	Unimodal	(010)[100]	0.132
DR538-R3	Natural	Olivine	Orthorhombic	29185	Bimodal	A-type with minor B-type; $(010)[100]$, $(010)[001]$	0.131
STO-2-03	Natural	Quartz	Trigonal	11671	Cross-girdle	Basal-a, rhomb-a, prism-a $(0001)\langle\bar{1}2\bar{1}0\rangle$, $\{10\bar{1}1\}\langle\bar{1}2\bar{1}0\rangle$, $\{0\bar{1}11\}\langle\bar{1}2\bar{1}0\rangle$ $\{10\bar{1}0\}\langle\bar{1}2\bar{1}0\rangle$	0.043
LVT128	Experimental	Calcite	Hexagonal	7155	Multimodal	Basal-a with ±rhomb slip; $(0001)\langle\bar{1}2\bar{1}0\rangle$, $\{10\bar{1}4\}\langle\bar{2}021\rangle$, $\{10\bar{1}4\}\langle20\bar{2}\bar{1}\rangle$	0.039
San466	Experimental	Quartz	Trigonal	7752	Multimodal	N/A	0.017

628

629

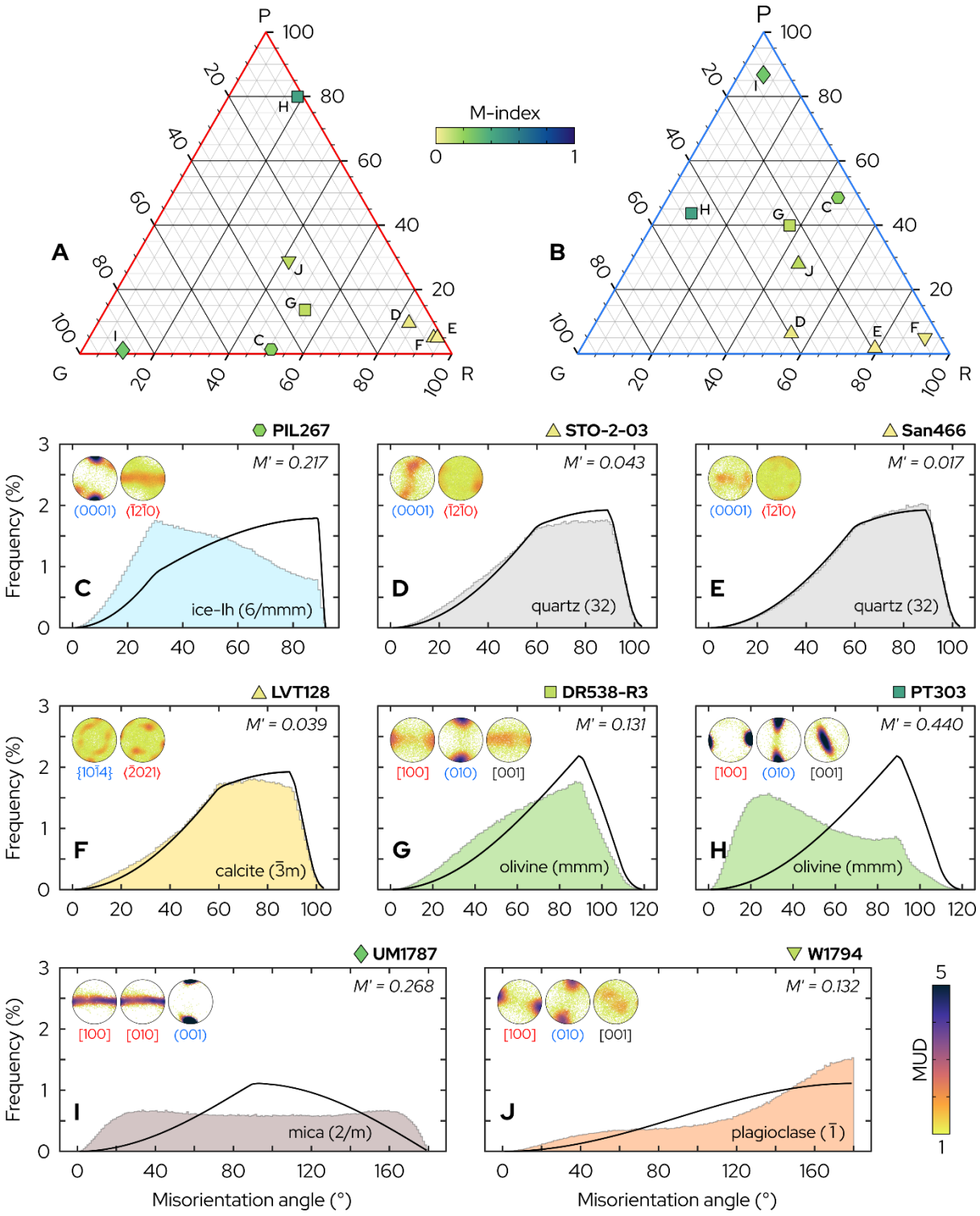

Figure 6: CPO intensity and symmetry of select natural and experimental samples. (A–B) Ternary plots, derived using the eigenvalue method of Vollmer (1990), showing the point-girdle-random CPO parameters of the inferred (A) Burgers vectors and (B) slip planes for each sample. Each symbol is coloured according to its M_{MAD} index value. (C–J) Random-pair misorientation angle histograms for

635 each sample (shaded), compared with the corresponding theoretical misorientation angle distribution
636 (black line) for the corresponding crystal symmetry class. The CPO of each sample is shown using
637 scattered pole figures (inset) where each data point is coloured by multiples of uniform distribution
638 (MUD). The pole figures are all lower-hemisphere, equal-area projections. Sample details are provided
639 in the main text.
640

641 Figure 7 shows the resampling analysis results for the natural and experimental specimens. As
642 expected, the probability of obtaining an M value within ±10% of the true, reference value, *M*′,
643 increases as more orientation measurements are provided. Furthermore, as shown for the VPSC
644 simulations, the number of measurements required to obtain an accurate value of *M* increases
645 with decreasing CPO intensity. For example, for the sample with the strongest CPO, PT303
646 (Figure 6H), there is a 95% probability of obtaining M within ±10% of *M*′ with only 300
647 orientation measurements (Figure 7A, squares), whereas ~2,000 measurements are required to
648 reach the same probability in sample San466, which has a near-random orientation distribution
649 (Figure 7A, upward-facing triangles).
650

651 Again, we can view these data in a more intuitive manner by plotting contoured heat maps of
652 the number of measurements required to obtain *M*′ within a certain probability. As shown in
653 Figure 7B, there is generally close correspondence between the heat map derived from the VPSC
654 simulations—taken as the average of Figures 5C and 5F, given their similarity—and the real
655 sample analyses. In general, the residual between the simulated and real data is within ±50%
656 (Figure 7C), where positive values indicate that more measurements are required for

convergence with M' than suggested by the VPSC simulations, and negative values indicate that fewer measurements are required for convergence. However, there are two notable exceptions. First, the strong (001)-fibre CPO of biotite in UM1787 can be accurately described with only half the number of measurements suggested by the VPSC analyses, likely because a fibre texture spans a continuous range of orientations rather than concentrating density within a small region of *SO(3)*, making the dominant fabric more readily sampled than a sharply localized unimodal distribution. Second, the very weak CPO of San466 requires far more measurements for an accurate representation of M than expected from the VPSC simulations—more than twice as many to obtain M' with > 90% probability (Figure 7C). This discrepancy ultimately reflects the precision with which M can be calculated—taking 10^6 random ODFs produces a range of M with mean, $\mu = 0.01$, and standard deviation, $\sigma = 0.001$. Thus, any CPO characterized by $M \leq 0.01$ should be considered effectively random (i.e., $M \approx 0$).

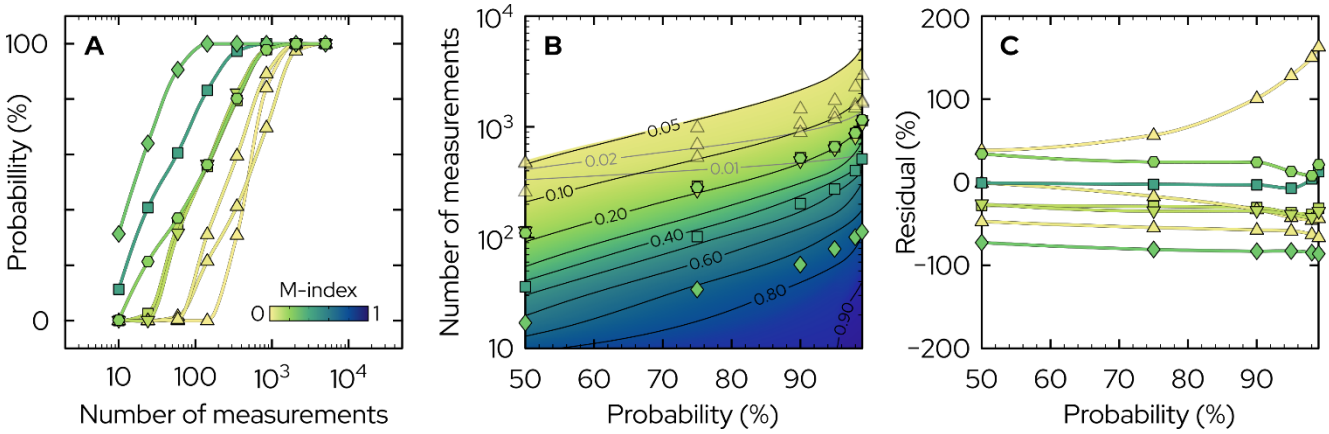

Figure 7: Resampling analysis for natural and experimental samples. (A) The probability of obtaining an estimate of *M* within 10% of the true CPO intensity, *M'*, as a function of CPO intensity and the number of orientation measurements. Symbol shapes and colours match those shown in Figure 6. (B) A contour plot showing the number of orientation measurements required to reach a certain probability of obtaining *M* within ±10% of *M'*. The heat map represents the average of Figures 5C and 5F, from the VPSC simulations. (C) The residual (i.e., misfit) between the VPSC results, represented by the heat map in (B), and the resampling analyses of the real specimens, represented by the symbols in (B). Positive values indicate that more measurements are required to obtain a measure of the "true" CPO intensity than is suggested by the VPSC simulations; negative values indicate that fewer measurements are required for a representative measure of *M* than the VPSC simulations would suggest.

For convenience, Figure 8 shows the heat map presented in Figure 7B replotted to show the number of measurements required to obtain a representative measure of M (± 10%) at varying levels of probability. Given that the VPSC simulations tend to overestimate the number of

687 measurements required for an accurate representation of *M*—note that most samples have
688 negative residuals in Figure 7C)—these values should be considered a conservative guide.
689

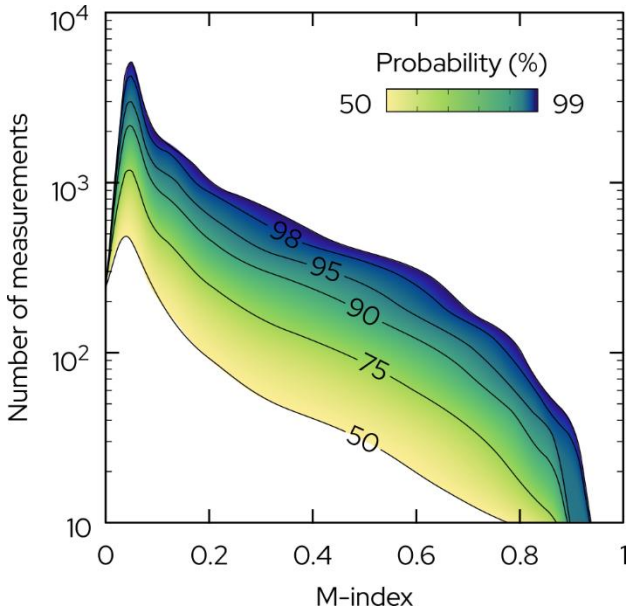

690

691 **Figure 8: General guidance for the number of measurements required to accurately measure CPO**
692 **intensity at various levels of probability.** Heat map derived from resampling analyses of the VPSC
693 simulations (i.e., Figures 5C and 5F). These values should be considered a conservative bound, as the
694 real (natural and experimental) samples analysed above show convergence at smaller population sizes.
695

696 **7. Sensitivity to map quality and grain reconstruction**

697 One of the main criticisms of the M-index, raised by Schaeben (2007), is that grain entities
698 must first be defined from spatially resolved orientation (map) data. Thus, the M-index may be
699 sensitive to map data quality (e.g., misindexing, clean-up methods) and user-defined grain
700 construction settings (e.g., the critical misorientation angle used to define grain boundaries).
701 Although this concern is not entirely justified—the M-index can also be reliably calculated

from non-spatially resolved orientation measurements, as uncorrelated (random-pair) misorientations are far more likely to be sampled than correlated (neighbour-pair) misorientations—we can nevertheless examine these potential sensitivities.

Figure 9 illustrates how M_{ODF} and M_{MAD} vary as a function of EBSD indexing rate and grain boundary misorientation angle for specimen DR538-R3, the abyssal peridotite mylonite described above (see also Figure 10A). For a given grain boundary misorientation angle (varied between 5° and 25°), we randomly selected 100 subsamples of *X*% indexed pixels (with *X* ranging from 10% to 80%), and constructed grains using only those pixels. This procedure generated 7,200 estimates of M_{MAD} and M_{ODF} each.

Generally speaking, the resampled values of M_{ODF} (Figure 9A) and M_{MAD} (Figure 9B) fall close to the reference values of 0.138 and 0.152, respectively, calculated using a grain boundary misorientation angle of 10° and all of the available indexed pixels (covering 86% of the map area). When expressed as residual percentages relative to these reference values, we find that M_{ODF} and M_{MAD} are largely insensitive to the critical misorientation angle used to define grain boundaries (Figures 9C, 9D). Indexing rate has a larger effect, producing deviations of up to ± 30% from the reference values, but narrowing to ± 5% when ≥ 50% of the mapped area is indexed (Figures 9C, 9D). Note, however, that the results shown in Figure 9 are generated for maps in which all of the non-indexed space is preserved. If we instead allow grain interpolation to fully fill all the non-indexed space, the residuals are much smaller, on the order of ± 10%

regardless of the indexing rate or grain boundary misorientation threshold (Supplementary Figure S3). Thus, the M-index appears relatively insensitive to map quality or processing workflow.

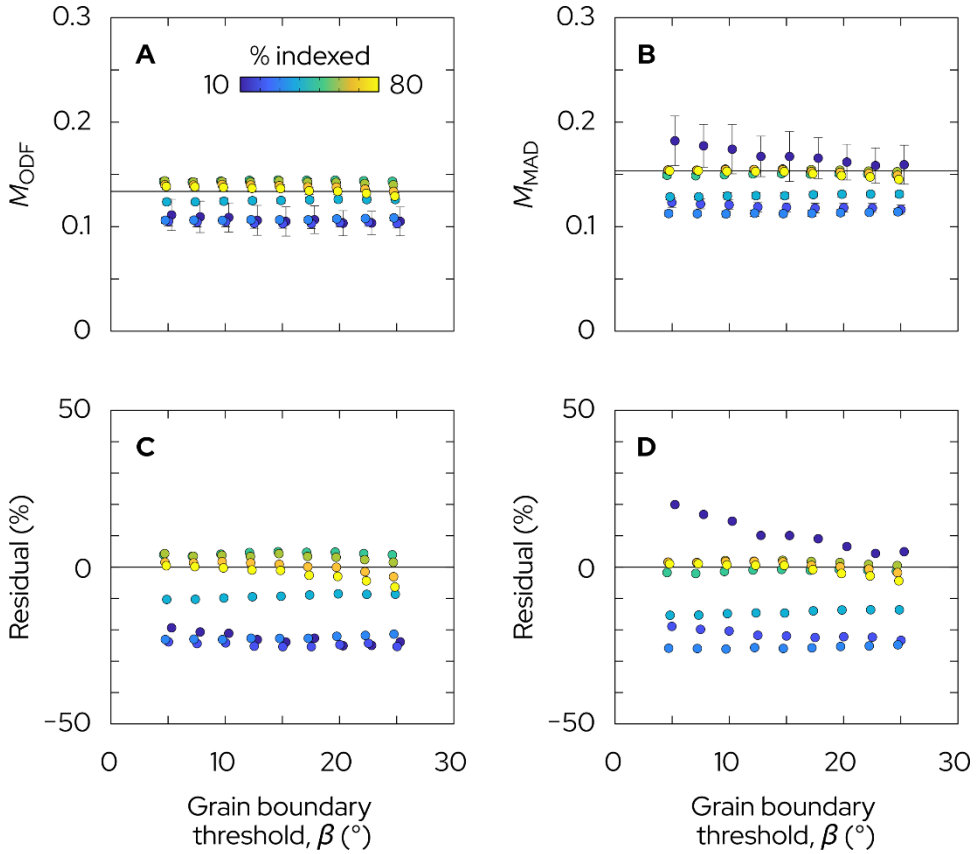

Figure 9: Effect of EBSD map quality (indexing rate) and grain construction (misorientation threshold). (A) M_{ODF} and (B) M_{MAD} as a function of grain boundary threshold misorientation (x-axis) and map indexing percentage (symbol colour). All non-indexed space was preserved during grain construction. The error bars indicate the 1σ variation among 100 randomly subsampled maps for each desired indexing percentage. The horizontal black lines indicate the reference (A) M_{ODF} and (B) M_{MAD} values calculated using all of the indexed pixels (which cover 86% of the map area) and a grain boundary misorientation threshold angle of 10°. (C–D) The residual of each (C) M_{ODF} and (D) M_{MAD} value, expressed as a percentage relative to their respective reference value.

8. One point per grain or all points?

Finally, when working with spatially resolved orientation data, another key consideration is whether to use all of the available data ("all points") or just one representative measurement per grain ("one point per grain"). In general, it is common practice to construct pole figures using only the one-point-per-grain data, particularly in specimens with bimodal grain sizes to avoid obscuring the overall CPO with the orientations of just a handful of large grains (e.g., Figure 10). Of course, one strategy is to explicitly subset each population of interest—based on grain size, grain shape, or microstructural domain, for instance—and plot those subpopulations separately. Indeed, this approach is preferable when each subpopulation is expected to have distinct physical properties. However, there are also scenarios in which it is useful to visualise the all-points data together, particularly when the area- or volume-weighted data have direct physical meaning—for example, when examining the bulk elastic (seismic) anisotropy of a given specimen.

Likewise, CPO intensity can be calculated using either the all-points or one-point-per-grain data. To illustrate the impact of this decision, we again examine specimen DR538-R3, which features a strongly bimodal grain size and modest A-type CPO. In Figure 10, we compare pole figures, misorientation angle distributions, and CPO intensities calculated for DR538-R3 using both the all-points (Figure 10B) and one-point-per-grain data (Figure 10C).

The all-points data for DR538-R3 produce distinct peaks at 2° and 65° misorientation angle (Figure 10B) due to the increased likelihood of sampling two orientations from within either of the two large olivine porphyroclasts. Consequently, the bulk A-type CPO becomes obscured and the all-points data produce an *M* value (M_{MAD} = 0.109) lower than that provided by the one-point-per-grain data (M_{MAD} = 0.131). However, it cannot be assumed that the all-points data will always produce lower CPO intensities than the one-point-per-grain data. Consider the case in which a coarse-grained, strongly textured aggregate contains a small fraction of fine, randomly oriented grains. In this case, the coarse-grained, area-dominant grain population will introduce bias towards larger CPO intensity values; thus, the all-points (area-weighted) data will yield a greater value of CPO intensity than the one-point-per-grain data.

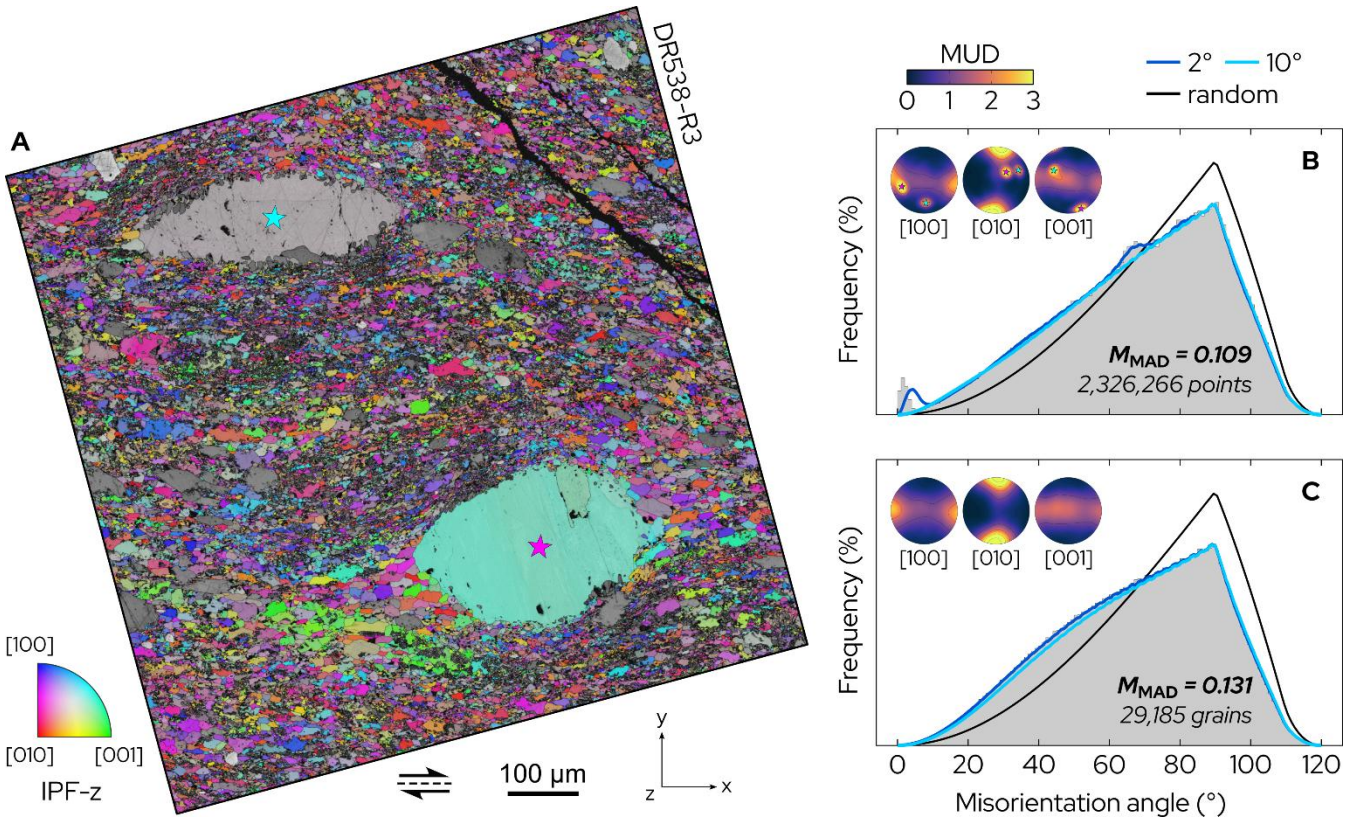

769 **Figure 10: Comparison of all-points versus one-point-per-grain CPO data for a porphyroclastic**
770 **abyssal peridotite mylonite, DR538-R3.** (A) An inverse pole figure (IPF) map showing crystal
771 orientations relative to the z-direction. (B–C) Random-pair misorientation angle histograms and
772 contoured pole figures for the (B) all-points and (C) one-point-per-grain data. The theoretical random
773 angle distribution is shown in black. For comparison, angle distributions derived from the ODF (Mainprice
774 et al., 2015) are shown for ODF kernel halfwidths of 2° (dark blue) and 10° (light blue).
775

776 Whatever the approach, it is also important to ensure that each subpopulation contains a
777 statistically robust number of measurements. This criterion is met for the fine-grained
778 population of DR538-R3, which is comprised of 29,183 grains—far exceeding the ~1,000
779 measurements needed to obtain a representative value of CPO intensity with 95% likelihood for
780 M_{MAD} = 0.13 (Figure 8). However, the same criterion is clearly not met for the coarse-grained
781 population in DR538-R3, which features only the two large porphyroclasts. If we assume for the
782 sake of demonstration that the coarse-grained population exhibits a similar CPO intensity of *M*
783 = 0.13 (and that the porphyroclasts are homogeneously distributed in space), an area ~500
784 times larger than that shown in Figure 10A would need to be analysed to achieve a similar level
785 of statistical robustness, equivalent to roughly one third of a standard 46 x 27 mm petrographic
786 thin section.
787

788 ## 9. Closing remarks and summary

789 Here we have evaluated the performance of two common measures of CPO intensity—the *J*-
790 index and the *M*-index—using synthetic, experimental, and natural datasets. Taken together,
791 these observations lead to the following practical recommendations:

- Scalar representations of the orientation density function (ODF)—namely, the J-index, and the M-index as currently implemented within MTEX—can be highly sensitive to the parameters used in their construction, including the kernel halfwidth and bandwidth, the kernel shape, and the method used to construct the ODF as a continuous function (e.g., Fourier decomposition or kernel superposition). While many of these sensitivities can be overcome with automatic kernel optimisation procedures such as those implemented within the MTEX open-source toolbox, similar optimisation procedures may not be available in proprietary software packages;
- ODF-derived metrics should not be compared without strict methodological consistency. Comparisons are only meaningful when calculation parameters (e.g., halfwidth, bandwidth, ODF construction method, symmetry treatment) are explicitly reported and held constant;
- The M-index provides a robust alternative. When calculated following the original formulation of Skemer et al. (2005)—that is, using the random-pair misorientation angle histogram—the M-index is computationally efficient, requires relatively few grain measurements for convergence, and yields stable, reproducible estimates of CPO intensity across a wide range of conditions. It is also largely insensitive to EBSD map quality and to the critical misorientation angle used for grain reconstruction.
- Monte Carlo resampling shows that CPO intensity can be accurately estimated using only ~500 individual orientations measurements for moderate-to-strong CPOs (M ≥ 0.25). However, for specimens with weak CPOs (i.e., M < 0.1), up to 3,000 measurements are

813 required—significantly greater than the number of measurements recommended by
814 Skemer et al. (2005), $N \leq 600$. Given the speed with which quantitative microstructure
815 data (e.g., EBSD data) can now be collected (e.g., Goulden et al., 2018), such population
816 sizes are easily attainable and should not be considered an obstacle to robust
817 microstructural analysis;

818 • When the volume-weighted data have direct physical meaning (e.g., seismic anisotropy),
819 CPO intensity should be calculated using all available orientation data (i.e., all points per
820 grain). Otherwise, one representative orientation per grain (e.g., the mean grain
821 orientation) may be preferable, particularly for specimens with strongly bimodal grain
822 sizes. In such cases, it may also be useful to analyse each distinct grain population
823 separately (e.g., large porphyroclasts versus small recrystallized grains). Regardless of the
824 approach, each distinct grain population must contain a statistically sufficient number of
825 measurements (based on the guidelines above).

826

827 For convenience, an MTEX-compatible function for calculating M via the original method of
828 Skemer et al. (2005) is included here (Supplementary Code S1) and contains functionality for
829 calculating M_{MAD} using either the all-points (EBSD pixel orientation) data or the one-point-per-
830 grain (mean grain orientation) data.

831

832 To close, the goal of this contribution is not to encourage the indiscriminate comparison of CPO
833 intensity among specimens of different crystal symmetry, CPO type (unimodal, multimodal,

fibre) or deformation history—such comparisons must always be approached with extreme caution. Rather, we aim to highlight the various sensitivities involved in CPO quantification, allowing the reader to make more deliberate, informed, and justified choices when reporting CPO data. By applying consistent methods, carefully reporting analytical procedures, and adopting stable metrics such as the M-index in its original form, the community can reduce ambiguity and make results more reproducible. Such practices will not only strengthen the comparability of studies within similar geological or experimental contexts, but also help build a more robust understanding of the processes recorded by CPO formation.

Acknowledgements

This work was supported by National Science Foundation (NSF) awards OCE-2224725 and OPP-2317263 to A.J.C, and additional salary support from an Anonymous Trustee Early-Career Fellowship to A.J.C. Permission to include unpublished EBSD data was graciously provided by Tim Schroeder and Frieder Klein (specimen DR538-R3), Subhajit Ghosh and Shivaji Saha (specimen UM1787), and Cameron Meyers and Greg Hirth (specimen W1794). Thanks to R. Graziani, M. A. Lopez-Sanchez, and an anonymous reviewer for thorough comments, and to P. Skemer and K. Billings for helpful discussions.

Author contributions

A. J. C. designed the study, performed the analyses, and wrote the manuscript.

Data availability

The EBSD maps for UM1787, W1794, DR538-R3, LVT128, STO-2-03 are publicly available at https://figshare.com/s/9e6687cfccf54478a4cc (to be made public upon acceptance of the article), the EBSD map for PT303 at https://doi.org/10.6084/m9.figshare.11838936.v1, the EBSD map for PIL267 at https://doi.org/10.6084/m9.figshare.13456550.v2, and the EBSD map for San466 at https://doi.org/10.6084/m9.figshare.29053211.v1. An MTEX-compatible function for calculating the M-index using the original MAD-based method of Skemer et al. (2005) is included as a supplementary file (Supplementary Code S1, "mIndexDiscrete.m").

References

Andrade, E. N. da C. and Roscoe, R. (1937). Glide in metal single crystals. Proceedings of the Physical Society, 49(2), 152.

American Society for Testing and Materials. (2013). Standard Practice for Determining Average Grain Size Using Electron Backscatter Diffraction (EBSD) in Fully Recrystallized Polycrystalline Materials. ASTM International.

Azuma, N. (1994). A flow law for anisotropic ice and its application to ice sheets. *Earth and Planetary Science Letters*, *128*(3-4), 601-614.

Bachmann, F., Hielscher, R., & Schaeben, H. (2010). Texture analysis with MTEX–free and open source software toolbox. *Solid state phenomena*, *160*, 63-68.

875 Barber, D. J., & Wenk, H. R. (1979). Deformation twinning in calcite, dolomite, and other
876 rhombohedral carbonates. Physics and Chemistry of Minerals, 5(2), 141-165.
877 Barreiro, J. G., Lonardelli, I., Wenk, H. R., Dresen, G., Rybacki, E., Ren, Y., & Tomé, C. N. (2007).
878 Preferred orientation of anorthite deformed experimentally in Newtonian creep. Earth
879 and Planetary Science Letters, 264(1-2), 188-207.
880 Boneh, Y., Morales, L. F., Kaminski, E., & Skemer, P. (2015). Modeling olivine CPO evolution with
881 complex deformation histories: Implications for the interpretation of seismic anisotropy
882 in the mantle. Geochemistry, Geophysics, Geosystems, 16(10), 3436-3455.
883 Bons, P. D., & den Brok, B. (2000). Crystallographic preferred orientation development by
884 dissolution–precipitation creep. Journal of Structural Geology, 22(11-12), 1713-1722.
885 Boogaart, K. G. v. d. (2001). Statistics for individual crystallographic orientation measurements.
886 PhD Thesis, TU Freiberg.
887 Boullier, A. M., & Gueguen, Y. (1975). SP-mylonites: origin of some mylonites by superplastic
888 flow. Contributions to Mineralogy and Petrology, 50(2), 93-104.
889 Bowman, A. W. (1984). An alternative method of cross-validation for the smoothing of density
890 estimates. Biometrika, 71(2), 353-360.
891 Bozzolo, N., Gerspach, F., Sawina, G., & Wagner, F. (2007). Accuracy of orientation distribution
892 function determination based on EBSD data-A case study of a recrystallized low alloyed
893 Zr sheet. Journal of microscopy, 227(3), 275-283.
894 Bunge, H. J. (1982). *Texture analysis in materials science: mathematical methods*. Butterworths.

895 Bystricky, M., Kunze, K., Burlini, L., & Burg, J. P. (2000). High shear strain of olivine aggregates:
896 Rheological and seismic consequences. *Science*, *290*(5496), 1564-1567.
897 Castelnau, O., Thorsteinsson, T., Kipfstuhl, J., Duval, P., & Canova, G. R. (1996). Modelling fabric
898 development along the GRIP ice core, central Greenland. Annals of Glaciology, 23, 194-
899 201.
900 Cross, A. J., Kidder, S., & Prior, D. J. (2015). Using microstructures and TitaniQ thermobarometry
901 of quartz sheared around garnet porphyroclasts to evaluate microstructural evolution
902 and constrain an Alpine Fault Zone geotherm. Journal of Structural Geology, 75, 17-31.
903 Cross, A. J., Hirth, G., & Prior, D. J. (2017a). Effects of secondary phases on crystallographic
904 preferred orientations in mylonites. Geology, 45(10), 955-958.
905 Cross, A. J., Prior, D. J., Stipp, M., & Kidder, S. (2017b). The recrystallized grain size piezometer
906 for quartz: An EBSD-based calibration. Geophysical Research Letters, 44(13), 6667-6674.
907 Cross, A. J., & Skemer, P. (2017). Ultramylonite generation via phase mixing in high-strain
908 experiments. Journal of Geophysical Research: Solid Earth, 122(3), 1744-1759.
909 Demurtas, M., Smith, S. A., Prior, D. J., Brenker, F. E., & Di Toro, G. (2019). Grain size sensitive
910 creep during simulated seismic slip in nanogranular fault gouges: Constraints from
911 transmission Kikuchi diffraction (TKD). Journal of Geophysical Research: Solid Earth,
912 124(10), 10197-10209.
913 Fan, S., Cross, A. J., Prior, D. J., Goldsby, D. L., Hager, T. F., Negrini, M., & Qi, C. (2021a).
914 Crystallographic preferred orientation (CPO) development governs strain weakening in

915 ice: Insights from high-temperature deformation experiments. Journal of Geophysical
916 Research: Solid Earth, 126(12), e2021JB023173.
917 Fan, S., Prior, D. J., Cross, A. J., Goldsby, D. L., Hager, T. F., Negrini, M., & Qi, C. (2021b). Using
918 grain boundary irregularity to quantify dynamic recrystallization in ice. Acta materialia,
919 209, 116810.
920 Fliervoet, T. F., Drury, M. R., & Chopra, P. N. (1999). Crystallographic preferred orientations and
921 misorientations in some olivine rocks deformed by diffusion or dislocation creep.
922 Tectonophysics, 303(1-4), 1-27.
923 Gilgannon, J., Freitas, D., Rizzo, R. E., Wheeler, J., Butler, I. B., Seth, S., Marone, F., Schlepütz, C. M.,
924 McGill, G., Watt, I., Plümper, O., Eberhard, L., Amiri, H., Chogani, A., & Fusseis, F. (2024).
925 Elastic stresses can form metamorphic fabrics. Geology, 52(3), 166-170.
926 Goddard, R. M., Cross, A. J., Lloyd, G., Breithaupt, T., Kumamoto, K. M., Dyck, B., Chen, H., Parsons,
927 A., Bidgood, A. (2025). A microstructural signature of the coesite-quartz transformation:
928 New insights from high-pressure experiments and EBSD. Earth and Planetary Science
929 Letters, 672, 119622.
930 Goulden, J., Trimby, P., & Bewick, A. (2018). The benefits and applications of a CMOS-based EBSD
931 detector. Microscopy and Microanalysis, 24(S1), 1128-1129.
932 Hansen, L. N., Zimmerman, M. E., & Kohlstedt, D. L. (2011). Grain boundary sliding in San Carlos
933 olivine: Flow law parameters and crystallographic-preferred orientation. Journal of
934 Geophysical Research: Solid Earth, 116(B8).

935 Hansen, L. N., Zimmerman, M. E., & Kohlstedt, D. L. (2012). Laboratory measurements of the
936 viscous anisotropy of olivine aggregates. Nature, 492(7429), 415-418.
937 Hansen, L. N., Conrad, C. P., Boneh, Y., Skemer, P., Warren, J. M., & Kohlstedt, D. L. (2016). Viscous
938 anisotropy of textured olivine aggregates: 2. Micromechanical model. Journal of
939 Geophysical Research: Solid Earth, 121(10), 7137-7160.
940 Hao, M., Pommier, A., Codillo, E. A., Walter, M. J., Cross, A. J., Hrubiak, R., Wagner, L., Thomson,
941 A. R., Yang, J., & Backhouse, N. (2024). Electrical conductivity and sound velocities of talc
942 under high pressure and high temperature conditions and application to the subducting
943 Cocos plate. Journal of Geophysical Research: Solid Earth, 129(11), e2024JB029824.
944 Hielscher, R., Schaeben, H., & Siemes, H. (2010). Orientation distribution within a single hematite
945 crystal. Mathematical Geosciences, 42(4), 359-375.
946 Humphreys, F. J. (2001). Review grain and subgrain characterisation by electron backscatter
947 diffraction. Journal of materials science, 36(16), 3833-3854.
948 Jura, J., Pospiech, J., & Gottstein, G. (1996). Estimation of the Minimum Number of Single Grain
949 Orientation Measurements for ODF Determination. International Journal of Materials
950 Research, 87(6), 476-480.
951 Karato, S. I. (1988). The role of recrystallization in the preferred orientation of olivine. Physics of
952 the Earth and Planetary Interiors, 51(1-3), 107-122.
953 Karato, S. I., Jung, H., Katayama, I., & Skemer, P. (2008). Geodynamic significance of seismic
954 anisotropy of the upper mantle: New insights from laboratory studies. *Annu. Rev. Earth*
955 *Planet. Sci.*, *36*(1), 59-95.

Klein, F., Schroeder, T., John, C. M., Davis, S., Humphris, S. E., Seewald, J. S., Sichel, S., Bach, W., & Brunelli, D. (2024). Mineral carbonation of peridotite fueled by magmatic degassing and melt impregnation in an oceanic transform fault. Proceedings of the National Academy of Sciences, 121(8), e2315662121.

Lebensohn, R. A., & Tomé, C. N. (1993). A self-consistent anisotropic approach for the simulation of plastic deformation and texture development of polycrystals: application to zirconium alloys. Acta metallurgica et materialia, 41(9), 2611-2624.

Lopez-Sanchez, M. A., & Llana-Fúnez, S. (2016). An extension of the Saltykov method to quantify 3D grain size distributions in mylonites. Journal of Structural Geology, 93, 149-161.

Lopez-Sanchez, M. A. (2020). Which average, how many grains, and how to estimate robust confidence intervals in unimodal grain size populations. Journal of Structural Geology, 135, 104042.

Mainprice, D., & Nicolas, A. (1989). Development of shape and lattice preferred orientations: application to the seismic anisotropy of the lower crust. *Journal of Structural Geology*, *11*(1-2), 175-189.

Mainprice, D., Bachmann, F., Hielscher, R., & Schaeben, H. (2015). Descriptive tools for the analysis of texture projects with large datasets using MTEX: strength, symmetry and components. *Geological Society, London, Special Publications*, *409*(1), 251-271.

Matthies, S., & Wagner, F. (1996). On a 1/n law in texture related single orientation analysis. physica status solidi (b), 196(2), K11-K15.

976 Meyers, C. D., Hirth, G., Cross, A. J., & Prior, D. J. (2013). The effect of dynamic recrystallization
977 and LPO formation on deformation mechanisms in experimentally deformed plagioclase
978 aggregates. In AGU Fall Meeting Abstracts (Vol. 2013, pp. T53A-2557).
979 Miranda, E. A., Hirth, G., & John, B. E. (2016). Microstructural evidence for the transition from
980 dislocation creep to dislocation-accommodated grain boundary sliding in naturally
981 deformed plagioclase. Journal of Structural Geology, 92, 30-45.
982 Miyazaki, T., Sueyoshi, K., & Hiraga, T. (2013). Olivine crystals align during diffusion creep of
983 Earth's upper mantle. Nature, 502(7471), 321-326.
984 Molinari, A., Canova, G. R., & Ahzi, S. (1987). A self-consistent approach of the large deformation
985 polycrystal viscoplasticity. Acta Metallurgica, 35(12), 2983-2994.
986 Pozzi, G., De Paola, N., Holdsworth, R. E., Bowen, L., Nielsen, S. B., & Dempsey, E. D. (2019).
987 Coseismic ultramylonites: An investigation of nanoscale viscous flow and fault weakening
988 during seismic slip. Earth and Planetary Science Letters, 516, 164-175.
989 Précigout, J., & Hirth, G. (2014). B-type olivine fabric induced by grain boundary sliding. Earth
990 and Planetary Science Letters, 395, 231-240.
991 Qi, C., Zhao, Y. H., Zimmerman, M. E., Kim, D., & Kohlstedt, D. L. (2021). Evolution of
992 microstructural properties in sheared iron-rich olivine. Journal of Geophysical Research:
993 Solid Earth, 126(3), e2020JB019629.
994 Rathmann, N. M., Mosegaard, K., Bekkevold, I. M., Lilien, D. A., & Prior, D. J. (2024). A spectral
995 directors method for modeling the coupled evolution of flow and CPO in polycrystalline
996 olivine. Geochemistry, Geophysics, Geosystems, 25(12), e2024GC011831.

997 Rutter, E. H., Casey, M., & Burlini, L. (1994). Preferred crystallographic orientation development
998 during the plastic and superplastic flow of calcite rocks. Journal of Structural Geology,
999 16(10), 1431-1446.
1000 Schaeben, H. (1988). Entropy optimization in quantitative texture analysis. Journal of Applied
1001 Physics, 64(4), 2236-2237.
1002 Schaeben, H. (1997). A simple standard orientation density function: The hyperspherical de la
1003 Vallée Poussin kernel. *Physica status solidi (b)*, *200*(2), 367-376.
1004 Schaeben, H. (2007). Comment on "The misorientation index: Development of a new method for
1005 calculating the strength of lattice-preferred orientation" by Philip Skemer, Ikuo Katayama,
1006 Zhenting Jiang, Shun-ichiro Karato. Tectonophysics, 441(1-4), 115-117.
1007 Shivaji, S. (2020). Tectono-metamorphic evolution of the Himalayan metamorphic rocks: Insights
1008 from the Mandakini and Madhmaheswar Ganga river valley, Northwestern India. *Doctoral*
1009 *dissertation*.
1010 Skemer, P., Katayama, I., Jiang, Z., & Karato, S. I. (2005). The misorientation index: Development
1011 of a new method for calculating the strength of lattice-preferred orientation.
1012 Tectonophysics, 411(1-4), 157-167.
1013 Skemer, P., & Karato, S. I. (2007). Reply to Comment on "The Misorientation index: Development
1014 of a new method for calculating the strength of lattice-preferred orientation".
1015 Tectonophysics, 441(1-4), 119-120.
1016 Skemer, P., & Hansen, L. N. (2016). Inferring upper-mantle flow from seismic anisotropy: An
1017 experimental perspective. *Tectonophysics*, *668*, 1-14.

1018 Skemer, P., Warren, J. M., Hansen, L. N., Hirth, G., & Kelemen, P. B. (2013). The influence of water
1019 and LPO on the initiation and evolution of mantle shear zones. *Earth and Planetary*
1020 *Science Letters*, *375*, 222-233.
1021 Skemer, P., Couvy, H., Cross, A. J., Littleton, J. A., & Bollinger, C. (2025). Large volume torsion
1022 (LVT) apparatuses for rock deformation at high pressure and temperature. Review of
1023 Scientific Instruments, 96(2).
1024 Shoji, H., & Langway Jr, C. C. (1988). Flow-law parameters of the Dye 3, Greenland, deep ice core.
1025 *Annals of Glaciology*, *10*, 146-150.
1026 Soda, Y., Harigane, Y., Kajimoto, K., & Okudaira, T. (2019). Crystallographic preferred orientations
1027 of plagioclase via grain boundary sliding in a lower-crustal anorthositic ultramylonite.
1028 International Journal of Earth Sciences, 108(6), 2057-2069.
1029 Smith, E. C., Baird, A. F., Kendall, J. M., Martín, C., White, R. S., Brisbourne, A. M., & Smith, A. M.
1030 (2017). Ice fabric in an Antarctic ice stream interpreted from seismic anisotropy.
1031 *Geophysical Research Letters*, *44*(8), 3710-3718.
1032 Sundberg, M., & Cooper, R. F. (2008). Crystallographic preferred orientation produced by
1033 diffusional creep of harzburgite: Effects of chemical interactions among phases during
1034 plastic flow. Journal of Geophysical Research: Solid Earth, 113(B12).
1035 Thomas, R., Cross, A. J., Prior, D. J., Fleming, M., & Palmer, M. (2024, December). Can superplastic
1036 creep produce a crystallographic preferred orientation (CPO) in ice?. In AGU Fall Meeting
1037 Abstracts (Vol. 2024, pp. C51A-09).

1038 Tokle, L., Hirth, G., & Behr, W. M. (2019). Flow laws and fabric transitions in wet quartzite. Earth
1039 and Planetary Science Letters, 505, 152-161.
1040 Tommasi, A., Mainprice, D., Canova, G., & Chastel, Y. (2000). Viscoplastic self-consistent and
1041 equilibrium-based modeling of olivine lattice preferred orientations: Implications for the
1042 upper mantle seismic anisotropy. Journal of Geophysical Research: Solid Earth, 105(B4),
1043 7893-7908.
1044 Tullis, J. (1970). Quartz: preferred orientation in rocks produced by Dauphiné twinning. Science,
1045 168(3937), 1342-1344.
1046 Tullis, J. A. (1979). High temperature deformation of rocks and minerals. Reviews of Geophysics,
1047 17(6), 1137-1154.
1048 Vollmer, F. W. (1990). An application of eigenvalue methods to structural domain
1049 analysis. *Geological Society of America Bulletin*, *102*(6), 786-791.
1050 Wagner, F., Matthies, S., & Van Landuyt, O. (1998). Processing individual orientation data to
1051 calculate ODFs. In Materials science forum (Vol. 273, pp. 89-98). Trans Tech Publications
1052 Ltd.
1053 Wenk, H. R. (2002). Texture and anisotropy. Reviews in mineralogy and geochemistry, 51(1), 291-
1054 329.
1055 Wheeler, J., Prior, D., Jiang, Z., Spiess, R., & Trimby, P. (2001). The petrological significance of
1056 misorientations between grains. *Contributions to mineralogy and petrology*, *141*, 109-124.
1057 Wheeler, J. (2009). The preservation of seismic anisotropy in the Earth's mantle during diffusion
1058 creep. Geophysical Journal International, 178(3), 1723-1732.

1059 Woodcock, N. H. (1977). Specification of fabric shapes using an eigenvalue method. *Geological*
1060 *Society of America Bulletin*, *88*(9), 1231-1236.
1061 Zhang, Y., Hobbs, B. E., & Jessell, M. W. (1994). The effect of grain-boundary sliding on fabric
1062 development in polycrystalline aggregates. Journal of Structural Geology, 16(9), 1315-
1063 1325.